THESIS FOR THE DEGREE OF LICENTIATE OF ENGINEERING

Defects in Bismuth Vanadate: Insights from First Principles

Nicklas Österbacka

Department of Physics
CHALMERS UNIVERSITY OF TECHNOLOGY
Göteborg, Sweden 2022

Defects in Bismuth Vanadate:
Insights from First Principles
Nicklas Österbacka

Department of Physics
Chalmers University of Technology
se-412 96 Göteborg, Sweden
Telephone +46 (0)31 772 10 00

Cover: A rendition of a vanadium vacancy in bismuth vanadate.

Chalmers digitaltryck
Göteborg, Sweden 2022

Defects in Bismuth Vanadate: Insights from First Principles

Nicklas Österbacka
Department of Physics
Chalmers University of Technology

Abstract

Photoelectrochemical water splitting is an attractive technique for sustainable hydrogen production, but its efficiency is heavily dependent on the properties of the semiconducting photoelectrodes used in the process. These properties are intimately connected to the presence of point defects in the materials, and understanding this relationship is a key step towards the development of better photoabsorbers. The effects of single impurities are challenging to probe using experimental techniques, but the use of computer modelling makes it possible to study modifications on the level of individual atoms. This thesis investigates native point defects in bismuth vanadate using hybrid density functional theory. The fundamentals of water splitting and the properties of the material are reviewed. Additionally, the theoretical foundations of the applied computational methods are described. The calculations performed within the thesis highlight the structural complexity of native point defects in bismuth vanadate and the important role that charge localization plays in its defect chemistry. In addition, it is found that oxygen vacancies induce significant lattice distortions at realistic concentrations. Simulated powder X-ray diffraction patterns reveal that this makes phase identification difficult.

Keywords: electronic structure theory, density functional theory, solar water splitting, bismuth vanadate, defect modelling, semiconductors, solar energy

LIST OF APPENDED PAPERS

This thesis consists of an introductory text and the following papers:

I **Influence of Oxygen Vacancies on the Structure of $BiVO_4$**
Nicklas Österbacka and Julia Wiktor
Journal of Physical Chemistry C **125**, 1200–1207 (2021)

II **Charge Localization in Defective $BiVO_4$**
Nicklas Österbacka, Francesco Ambrosio and Julia Wiktor
Journal of Physical Chemistry C **126**, 2960–2970 (2022)

The author's contribution to the papers:

I The author performed the calculations, analysis and preparation of figures and wrote the paper.

II The author performed most of the calculations. The author additionally performed analysis of results, preparation of figures and wrote the paper.

PUBLICATIONS NOT INCLUDED IN THIS THESIS

The following publications are outside the scope of this thesis:

Small Electron Polarons in $CsPbBr_3$:
Competition between Electron Localization and Delocalization
Nicklas Österbacka, Paul Erhart, Stefano Falletta, Alfredo Pasquarello and Julia Wiktor
Chemistry of Materials **32**, 8393–8400 (2020)

Contents

List of abbreviations

ms monoclinic scheelite. 9, 14, 31

ts tetragonal scheelite. 9, 13

ADMM Auxiliary Density Matrix Method. 26

CBM conduction band minimum. 5, 6, 9

DFT density functional theory. 16, 17, 19, 24, 26–28

GGA generalized gradient approximation. 18, 19, 24

GPW Gaussian and Plane Waves. 25

HER hydrogen evolution reaction. 3, 6, 9

HF Hartree-Fock. 18–20, 22, 24–26

HK Hohenberg-Kohn. 16, 17

KS Kohn-Sham. 17, 20–25

LDA local density approximation. 18

OER oxygen evolution reaction. 3–7, 9, 10, 12, 13, 33

PBE Perdew-Burke-Ernzerhof. 18, 19, 25, 26

PEC photoelectrochemical. 5–7, 9, 10, 12, 13, 33

PES potential energy surface. 16

SHE standard hydrogen electrode. 4

SIE self-interaction error. 18

VBM valence band maximum. 5–7, 9, 27

XC exchange-correlation. 17–20, 23, 25

1

Introduction

With the climate crisis fast approaching, in large parts owing to emissions stemming from the transport and manufacturing sectors, the use of fossil fuels must be phased out promptly. Societal energy needs are not decreasing, however, so alternatives must be found to take their place. The ”hydrogen economy” has been lauded as a partial replacement to the current hydrocarbon-based energy economy, which is an attractive option on paper; hydrogen has a relatively high energy density, and its use in a fuel cell produces nothing but water. As hydrogen can be produced by splitting water, sustainable production of the fuel is in principle possible. However, the associated chemical reaction is highly endothermic, and the viability of the approach thus requires the ability to provide this energy in a sustainable fashion.

As shown by Fujishima and Honda in 1972, [1] the reaction can be driven using sunlight as an energy source, as long as an appropriate semiconducting photocatalyst is used. Although the device they constructed was inefficient, their demonstration sparked a significant research interest in photoelectrochemical water splitting. Despite steady progress since then, the practical efficiency of the process is still limited and remains well below what is theoretically achievable. As a result, widespread commercial adaption is yet to come. Some materials have nevertheless been identified as good candidates, and have thus received the bulk of the attention from the scientific community.

This thesis focuses on one such candidate: bismuth vanadate, a complex metal oxide semiconductor. Its potential as a water-splitting photocatalyst was first highlighted by Kudo *et al.* in 1998 [2] and it remains one of the best contenders to this very day. [3] The efficiencies of bismuth vanadate-based water splitting devices have so far been undesirably low, as the material exhibits relatively low charge conductivity and a bandgap slightly larger than what would be ideal. An atomistic understanding of the underlying connection between materials structure and properties is key to solving these issues, but unravelling this relationship is far from trivial.

Most materials are imperfect, which further complicates matters: atoms might be missing in places, or there may be impurities present. These are called *point defects* and are, as the name implies, often undesirable due to a detrimental effect on the properties of the material. This is not always the case, however, as they are key to the usefulness of many semiconductors. In such cases, careful control of their nature and abundance is necessary to achieve the desired behaviour.

Bismuth vanadate is no exception to this. Two studies on defects in the material make up the foundations of this thesis, which aims to provide insight into the role that native defects play in defining the structure and properties of the semiconductor by means of first-principles modelling.

1.1 Thesis outline

Chapter 2 gives a brief overview of the mechanics of water splitting through electrochemical and photoelectrochemical means. The chapter ends with a few examples of materials that have been identified as promising photocatalysts to drive the reaction. Chapter 3 focuses on bismuth vanadate. Its properties and limitations are introduced, as well as several routes to improve them that have been explored in the literature. The fundamentals of the first-principles methods used in the papers are reviewed in Chapter 4, which is wrapped up with a brief explanation of some techniques applied to reduce the computational complexity of the calculations. This thesis involved modelling of defects, which require special care if they are charged; a method for dealing with this is outlined in Chapter 5. Finally, a summary of the papers that are included in the thesis is given in Chapter 6 and a brief outlook for the future is given in Chapter 7.

2

Water splitting

As society gradually transitions from reliance on fossil fuels, the need for clean and sustainable alternatives is growing. Hydrogen is a good candidate, as it can be produced from water through the reaction

$$2\,H_2O \longrightarrow 2\,H_2 + O_2. \tag{2.1}$$

The reverse reaction occurs when hydrogen is used as a fuel, producing water. This water splitting reaction is highly endothermic, however, with a Gibbs free energy difference of ~ 4.92 eV between reactants and products at standard conditions. [4] The energy required is even higher in practice due to process inefficiencies. As a result, extensive efforts have been made to minimize any losses in the reaction.

In this chapter, a brief introduction is given to the concept of electrochemical water splitting. Photoelectrochemical water splitting is then discussed, along with the material requirements to make it practical. Finally, a few materials that have shown promise as electrode materials for water splitting are presented.

2.1 Electrochemical water splitting

In electrochemical water splitting, or electrolysis of water, the requisite energy to drive the reaction in Eq. (2.1) is provided by applying an external voltage between two electrodes immersed in an aqueous electrolyte. The reaction is then effectively split into two redox half-reactions: the hydrogen evolution reaction (HER) on the cathode,

$$2\,H^+ + 2\,e^- \rightleftharpoons H_2,\ E^\circ = 0\ \text{V}, \tag{2.2}$$

and the oxygen evolution reaction (OER), or water oxidation reaction, on the anode,

$$2\,H_2O \rightleftharpoons 4\,H^+ + 4\,e^- + O_2,\ E^\circ = 1.23\ \text{V}. \tag{2.3}$$

Here, E° is the standard electrode potential referred to the standard hydrogen electrode (SHE) for the relevant redox couple, i.e., H^+/H_2 and H_2O/O_2. [5]

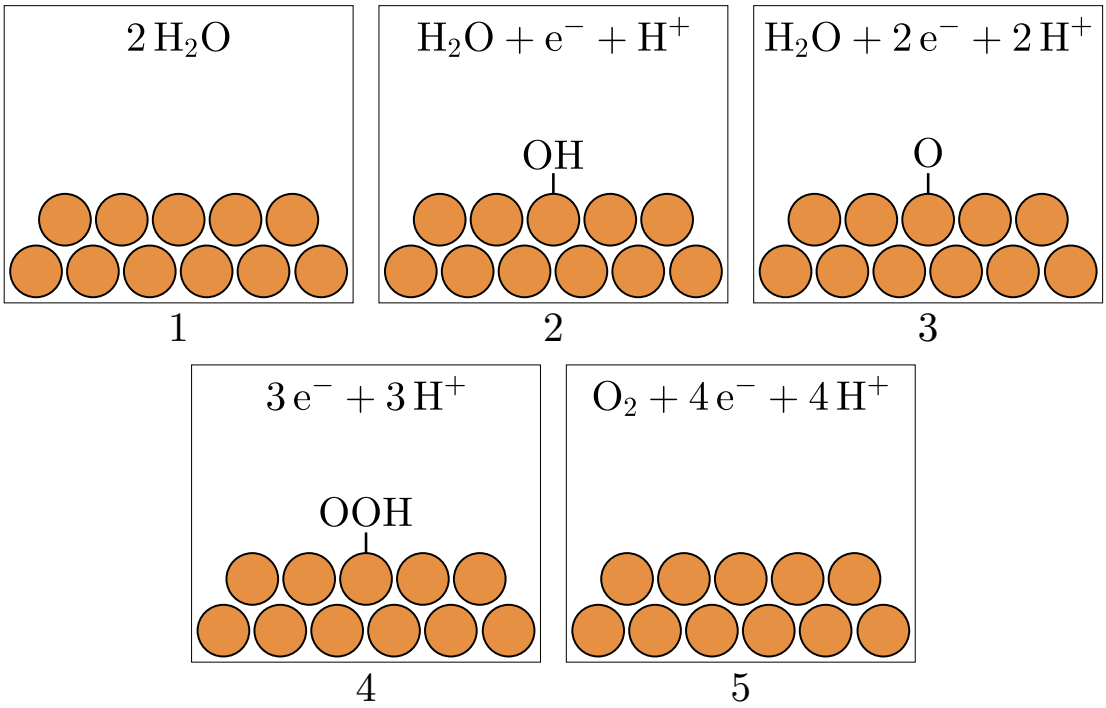

Figure 2.1: Surface-mediated OER reaction path in acidic conditions.

The overall bottleneck in water splitting is typically considered to be the OER, [5, p. 370] as its kinetics are limited by the need of transferring four holes across the semiconductor–electrolyte interface. The conventional OER pathway under acidic conditions is shown in Fig. 2.1. [5, 6] The overall free energy difference of the OER is 4.92 eV, which should ideally be split evenly amongst the reaction steps as shown by the red line on the left side of Fig. 2.2. Reversibility will then be achieved by applying a bias voltage of 1.23 V, bringing all of the intermediates into equilibrium. This is not sufficient to make the overall reaction favorable in practice, however. The right side of Fig. 2.2 shows a more realistic example, where one reaction step is associated with a significantly higher energy than the others; a barrier thus remains at the reversible potential of 1.23 V. Instead, a bias of 2.55 V is required to bring all intermediates into equilibrium. The difference between the reversible and practical bias requirements is called an overpotential, and should be minimized to maximize the efficiency of the reaction. The diagrams in Fig. 2.2 only take the free energy differences between the surface–adsorbate complexes into account, but factors such as kinetic barriers for the reactions and inefficient charge transfer to the electrolyte also contribute. Choosing an

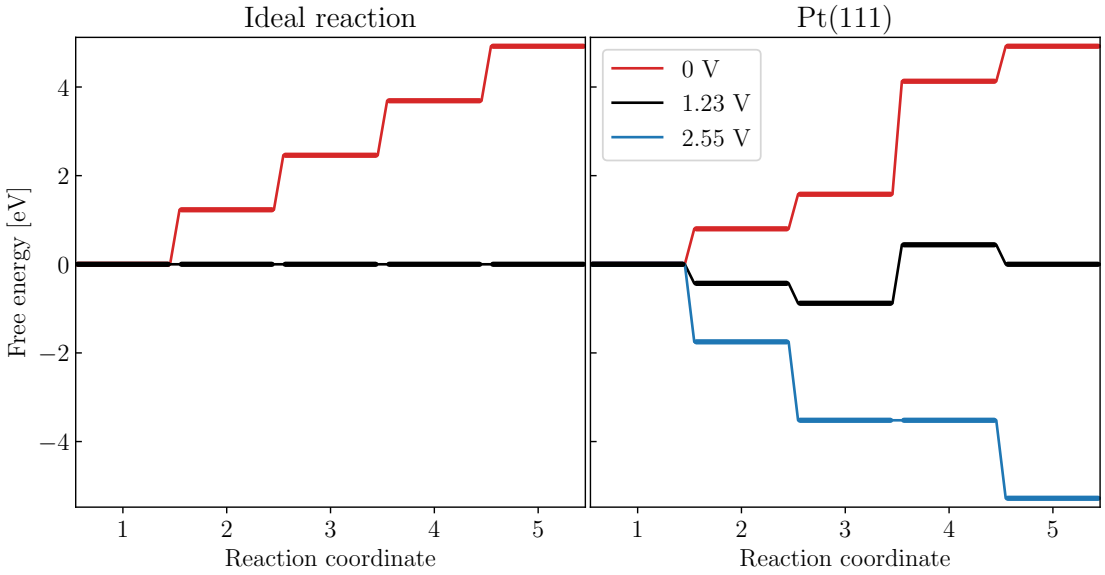

Figure 2.2: Schematic free energy diagram for the OER pathway of Fig. 2.1 for the reaction on (left) an ideal surface and (right) a pristine Pt(111) surface. The latter is based on calculations by Rossmeisl *et al.* [7] The application of a bias reduces the free energy for each intermediate step by the number of transferred electrons times the voltage.

appropriate catalyst material to support the intermediate reactions is key to efficient water splitting.

2.2 Photoelectrochemical water splitting

The need for an external voltage source limits the usefulness of electrolysis-based water splitting schemes; electricity generation incurs additional losses, which reduces the overall efficiency of the process. Furthermore, the environmental benefits of hydrogen as a fuel are greatly diminished when the impact of power production is taken into account. These issues can be circumvented by utilizing solar energy to drive the reaction, either through combined photovoltaic–electrolysis systems [8] or through photoelectrochemical (PEC) water splitting schemes.

The principles underlying PEC water splitting are essentially the same as those for electrolysis of water, the key difference being how the energy to drive the reaction is provided. Rather than relying on an external voltage source, the PEC approach relies on photoexcitation in a semiconductor. To make this possible, the band edges of the material must straddle the redox potentials for the two water splitting half-reactions; in other words, its conduction band minimum (CBM) must be more negative than $E^\circ(\mathrm{H^+/H_2})$ and its valence band maximum (VBM) more positive than $E^\circ(\mathrm{H_2O/O_2})$,

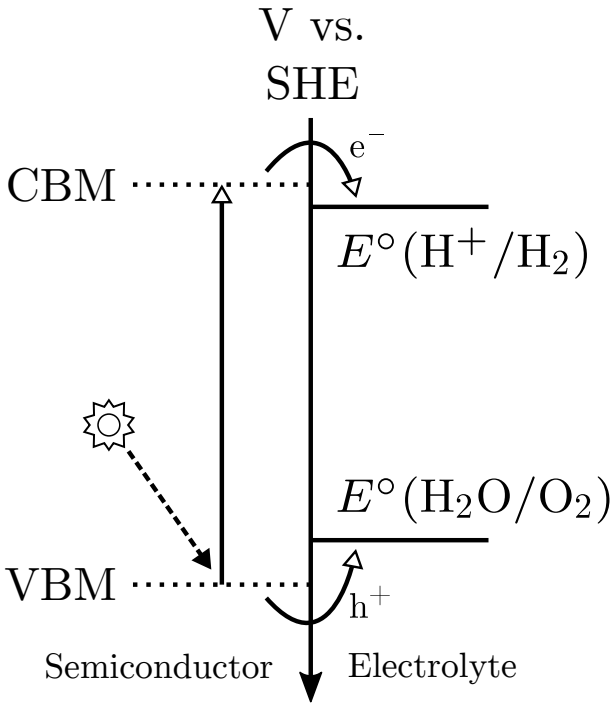

Figure 2.3: Schematic illustration of band alignment for PEC water splitting.

as illustrated in Fig. 2.3. Absorption of incident light causes electrons at the VBM to be excited to the CBM, leaving holes behind in the process. These charges can then participate in the HER and OER upon transfer to the electrolyte. While a bandgap of at least 1.23 eV is required to achieve the reversible situation depicted in Fig. 2.2, this is inadequate to drive the overall reaction in practice due to overpotential losses; the practical minimum is $\sim$1.6–2.0 eV. [5, 9]

Finding a semiconductor that simultaneously exhibits appropriate band edge alignment and a sufficiently large bandgap to drive the overall water splitting reaction is challenging. This can be made somewhat easier considering each half-reaction individually, which additionally allows for the optimization of materials for the HER and OER separately. This also makes the construction of composite devices possible, making higher solar-to-hydrogen efficiencies achievable. [10] While the practical realization of unassisted solar water splitting still eludes the scientific community, it remains an active field of research and several promising candidate materials for both half-reactions have been discovered. [9, 11, 12]

Cu_2O exhibits a bandgap of $\sim$2 eV and a CBM $\sim$0.7 eV more negative than the H^+/H_2 redox potential, [13, 14] allowing the semiconductor to absorb a large portion of the visible light spectrum and drive the HER unassisted. Unfortunately, the material is

susceptible to photodecomposition under working conditions as the redox potentials for reduction to Cu and oxidation to CuO lie within the bandgap. [13, 14] This limits the potential of the semiconductor for practical applications as a water-splitting photocathode, but its stability can be significantly enhanced by the deposition of protective overlayers. [15, 16]

TiO_2 was the first photoanode material used for the OER, [1] and remains the subject of intense research on its applications as a water splitting photoelectrode for both half-reactions. [17–19] Its usefulness as the main photoabsorber is limited as it exhibits a bandgap of ~ 3 eV, severely restricting its ability to absorb light in the visible regime. Strategies to overcome this limitation have been developed; for instance, incorporation of nitrogen significantly narrows the bandgap to enable visible-light absorption, [20, 21] although the resulting material exhibits very low water splitting PEC activity. Additionally, cobalt-based nanoclusters act as visible-light photosensitizers when deposited on the surface of rutile TiO_2 and additionally act as catalysts for the OER. [22, 23] Such modifications are key in making the material viable for water splitting devices.

For the OER, one of the best candidate materials is bismuth vanadate, $BiVO_4$. It exhibits good absorption of visible light owing to its bandgap of ~ 2.4 eV and favorable VBM position. [24, 25] Just as for Cu_2O and TiO_2, the material's viability as a water splitting photoelectrode is limited without significant modification; as $BiVO_4$ is the subject of both **Paper I** and **Paper II**, a deeper discussion of its properties and limiting factors is presented in Chapter 3 rather than here.

3

Bismuth vanadate

Bismuth vanadate, $BiVO_4$, is a promising photoelectrode for the water splitting reaction. It has been synthesized in several forms, but only the monoclinic scheelite (*ms*) phase, of spacegroup $I2/b$, and the tetragonal scheelite (*ts*) phase, of spacegroup $I4_1/a$, are of relevance to this thesis. [24, 26] Their crystal structures, illustrated in Fig. 3.1, consist of layers of VO_4 tetrahedra connected through BiO_8 polyhedra. The *ms* form can be described as a distortion of the *ts* form, as the former exhibits two distinct V – O bond lengths; these distortions are too subtle to be visible in Fig. 3.1, so only one structure is shown. Despite the structural similarity of the two phases, the *ms* form exhibits significantly higher PEC activity for the OER. [24, 27] As such, the rest of this chapter concerns *ms* $BiVO_4$ unless otherwise noted.

3.1 Properties, problems and solutions

$BiVO_4$ is considered to be an *n*-type semiconductor and exhibits an indirect bandgap of 2.4–2.5 eV, enabling absorption of a large part of the visible light spectrum. Its CBM lies just short of the $2\,H^+ + 2\,e^- \rightleftharpoons H_2$ redox potential, in principle making it possible to drive the HER with a moderate external bias, while its VBM lies well below the $2\,H_2O \rightleftharpoons 4\,H^+ + 4\,e^- + O_2$ redox potential, providing enough overpotential to drive the OER. [24, 28] For this reason, research has primarily concerned the material's utilization as a photoanode for the water oxidation half-reaction. The PEC efficiency of $BiVO_4$-based devices is lower than desired, however, as it is limited by high charge recombination, slow reaction kinetics and poor charge conductivity. [24, 25, 29] Fortunately, several ways of mitigating these issues have been explored in the literature.

The poor OER kinetics on $BiVO_4$ have been attributed to slow hole transport across the photoanode–electrolyte interface, [24] which increases charge recombination. To

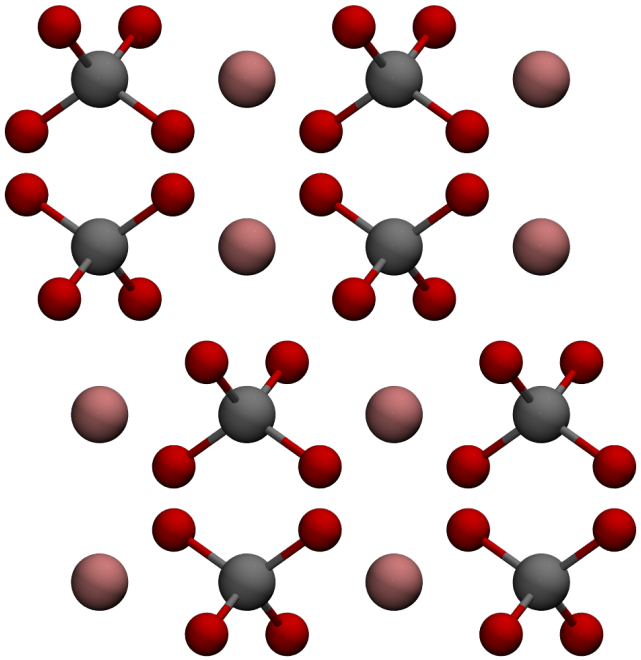

Figure 3.1: The crystal structure of scheelite $BiVO_4$. Bismuth atoms are shown in pink, vanadium in grey, and oxygen in red.

remedy this, OER catalysts can be deposited onto the surface to improve the reaction kinetics and hole transfer properties. For instance, cobalt phosphate has successfully been used for this purpose, significantly improving the PEC efficiency upon its addition. [30–32]

Photocharging is another PEC efficiency-improving technique that works through deposition of material onto the surface of $BiVO_4$. Under working conditions, OER photoanodes are immersed in electrolyte to regulate pH. Anions from this solution may adsorb to the surface upon illumination, forming an overlayer. With phosphate- and borate-based pH buffers this results in the formation of a heterojunction with $BiVO_4$, enhancing charge separation and suppressing charge recombination. [33–35] This effect is reversible, with the overlayer eventually dissolving in the dark.

Combining $BiVO_4$ with other materials in composite devices can also serve to circumvent the aforementioned shortcomings. For instance, $BiVO_4/WO_3$ composites have shown a significantly increased PEC efficiency compared to the individual materials. Of the two semiconductors, $BiVO_4$ more readily absorbs visible light, while the WO_3–electrolyte interface exhibits better charge transfer characteristics. [36–38] The device is thus able to make use of the advantages of both materials, while also improving charge separation thanks to the formation of a heterojunction. There is no strict need for both components to be semiconducting, however, as carbon nanotubes and graphene

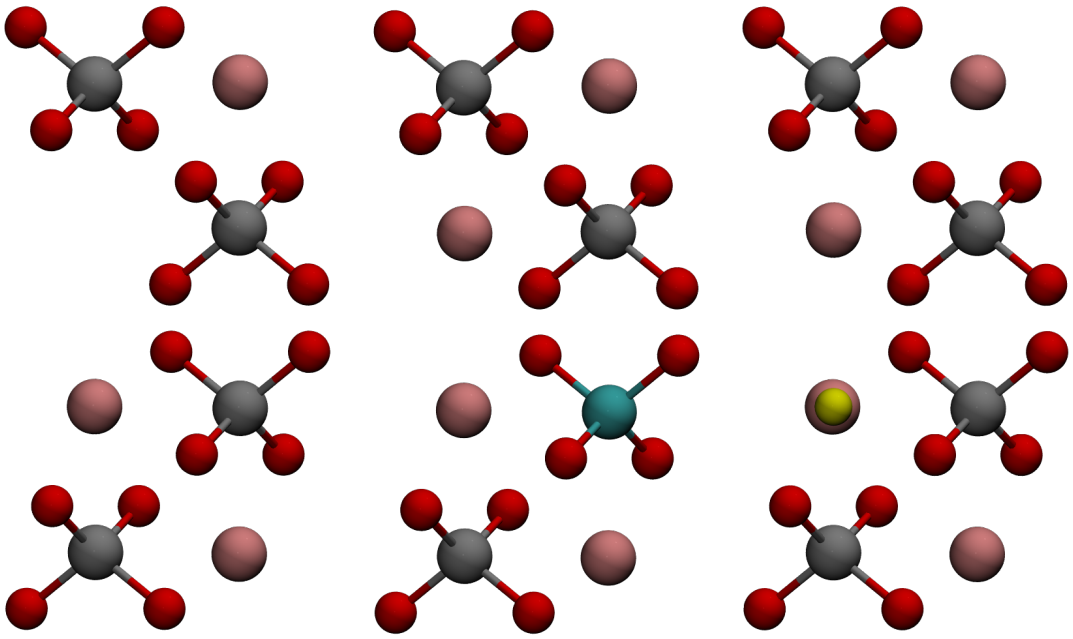

(a) Vacancy. **(b)** Substitutional atom. **(c)** Interstitial atom.

Figure 3.2: Illustrations of a) bismuth vacancy, b) substitutional, and c) interstitial defects in $BiVO_4$. The substitutional atom is shown in cyan, the interstitial in yellow, vanadium in grey, bismuth in pink, and oxygen in red.

have successfully been coupled to $BiVO_4$ in a similar fashion. [39, 40] Bismuth vanadate is then used as a medium for photoexcitation of charges, while the carbon-based material improves the charge conductivity of the photoanode.

3.2 Point defects in $BiVO_4$

Both intentional and unintentional modification of the material itself through changes in its atomic composition can also have a profound effect on its properties. This occurs through the formation of point defects, which may be divided into three classes as illustrated in Fig. 3.2: vacancies, where an atom is removed from the lattice, substitutional defects, where an atom is replaced with another type, and interstitials, where an atom is placed at an unoccupied site in an otherwise pristine host material. The figure shows the defects without lattice relaxations for the sake of clarity. In practice, the presence of the defect induces distortions in the surrounding lattice.

Doping, a common method for tailoring the properties of semiconductors, involves the intentional introduction of impurities to a material in the form of substitutional or interstitial defects. For instance, incorporation of tungsten and molybdeneum im-

proves charge separation, [41–43] while lithium enhances electron conductivity in the bulk of the material. [44] The overall effect of such impurities on the PEC efficiency of photoanodes is not always obvious nor beneficial, however; [24] tungsten has also been reported to decrease charge carrier mobility through the introduction of charge trap states. [45] The term ”doping” is typically reserved for cases where the inclusion has an overall beneficial effect. Both Kim *et al.* and Irani *et al.* studied nitrogen incorporation into $BiVO_4$ and found that this reduces the bandgap of the material. [46, 47] Only the former found that the overall effect on the PEC efficiency for the OER was beneficial, however, and the latter study does not refer to nitrogen as a dopant.

Native defects, i.e., those involving only the constituent atoms of the host, can also play a significant role in defining the properties of a material. The n-type conductivity of $BiVO_4$ has been attributed to the formation of oxygen vacancies, and research has had a particular focus on this type of defect. [48] Their abundance has been reported both to have a beneficial [49–51] and a detrimental [52–54] effect on the PEC activity of the material. This contradiction may have its explanation in differing behaviour of the defect in the bulk and at the surface, with the latter more likely to positively influence the OER. [55–57] Additionally, it has been suggested that the creation and subsequent annihilation of oxygen vacancies could play a direct part in the OER both on $BiVO_4$ and other transition metal oxides; [58–60] theoretical predictions by Nikačević *et al.* indicate that this alternative reaction path is unfavorable on $BiVO_4$, however. [61]

Cation vacancies have also been deemed important to the PEC efficiency of $BiVO_4$ photoanodes, but they have been studied less extensively. Lu *et al.* found that bismuth vacancies enhance the charge transfer properties of the material, thus benefiting the OER, [62] and theoretical predictions suggest that they are the dominant acceptor defects in the material. [63–65] Vanadium vacancies, on the other hand, have been found to be detrimental [53, 66] and to be a sign of photocorrosion through V^{5+} loss to the electrolyte. [67]

$BiVO_4$ exhibits strong localization of excess charges; rather than occupying delocalized states in the conduction and valence bands, electrons and holes tend to localize into small polarons centered on a lattice site, inducing structural distortions in their vicinity. This is illustrated for the pristine material in Fig. 3.3. As a consequence, charge conduction in the material is primarily realized through polaron hopping rather than band-mediated drift currents, which plays a part in the low carrier conductivity in the material. [68–70] Theoretical predictions by Wiktor *et al.* suggest that their presence at the $BiVO_4$–water interface affects band alignment and hampers the water splitting reaction, [71] though their precise role in the OER is yet to be established. The tendency to form polarons drastically affects the nature of point defects as well; they tend to act as electron acceptors or donors, and are able to interact with excess charges in the lattice. [72] A proper analysis of their effects must thus take this phenomenon into account.

No matter their effect, positive or negative, on the OER PEC performance of $BiVO_4$,

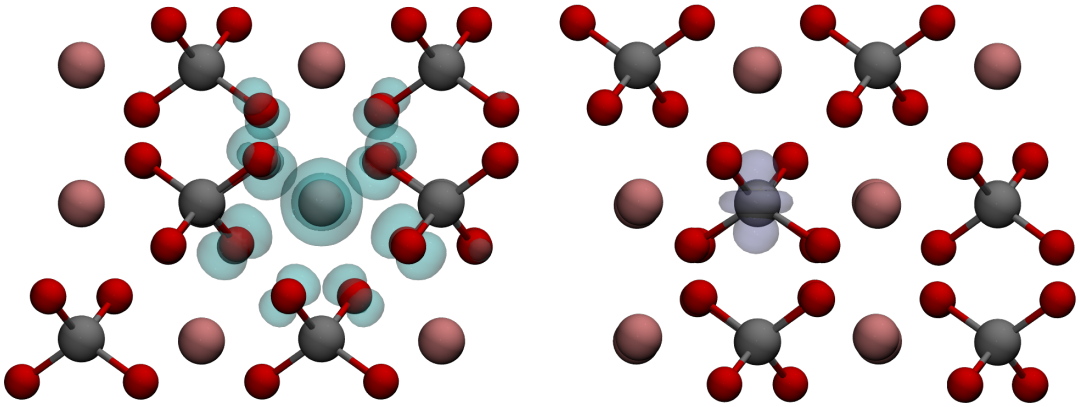

(a) Hole polaron. **(b)** Electron polaron.

Figure 3.3: Polarons in $BiVO_4$. Isosurfaces illustrate localization of an excess a) hole and b) electron.

controlling the abundance of point defects is of clear importance. This can be achieved by careful adjustment of conditions during synthesis and post-synthesis treatment. For example, annealing in N_2 or H_2 has been reported to result in the incorporation of nitrogen and hydrogen defects, respectively. [46, 73]. Similarly, annealing in O_2 suppresses the formation of oxygen vacancies, [55] while annealing in an oxygen-free inert gas encourages their formation. [74] Subjecting samples to high heat both during and after synthesis may additionally lead to vanadium loss, i.e., vacancy formation, unless additional vanadium is supplied during the procedure. [53, 66] The choice of synthesis precursor is also highly important; for instance, the use of vanadyl acetylacetone, $V(acac)_2$, as a vanadium source reportedly results in oxygen-deficient samples. [75, 76]

Point defects in $BiVO_4$ remain an active area of research, but isolating their effects can be difficult experimentally; in practice, several factors may simultaneously influence the performance of the material. For instance, the electrolyte may interact with the surface, as mentioned earlier, and maintaining perfect stoichiometry is challenging. The use of theoretical methods makes this the study of single defects possible, however. For example, electronic structure calculations have been used to support the notion that near-surface oxygen vacancies have a positive influence on the OER PEC performance of $BiVO_4$ by reducing the requisite overpotentials required to drive the reaction. [61] In **Paper I**, we simulate the effects of oxygen vacancies in *ts* $BiVO_4$ and find that they induce structural distortions that make phase identification difficult. [77] The theoretical foundations for the first-principles methods used in this thesis are outlined in Chapter 4.

A common theoretical approach is to calculate the formation energies of point defects to assess their stability and effects on conductivity under different synthesis conditions; the methodology is described in Chapter 5. Yin *et al.* and Zhang *et al.* performed such

an analysis for the native defects of $BiVO_4$ and found that the *ms* phase should exhibit p-type conductivity under a wide range of conditions, in stark contrast to the available experimental literature. [63, 64] This is likely due to the fact that their methodology fails properly describe charge localization. In **Paper II**, we take this phenomenon into account in a similar study, finding that p-type conductivity is difficult to achieve. [65]

4

Electronic structure theory

This chapter gives a very brief outline of the electronic structure methods used in this thesis. The formalism as it is presented closely follows that of Guistino's *Materials Modelling using Density Functional Theory*, [78] supplemented with Jensen's *Introduction to Computational Chemistry*, [79] as well as Koch's and Holthausen's *A Chemist's Guide to Density Functional Theory*. [80] As such, detailed references are omitted, although citations of the original work underlying the theory are included where appropriate. Some sections, such as that on the necessity of hybrid functionals, go beyond what is discussed in the books mentioned above. In such cases, additional references are included.

4.1 The Schrödinger Equation and Born-Oppenheimer approximation

The central quantity in quantum mechanics is the time-independent Schrödinger equation,

$$\mathcal{H}\Psi = E_{\text{tot}}\Psi, \tag{4.1}$$

with Hamiltonian operator $\mathcal{H}$, wavefunction Ψ and energy eigenvalue E_{tot}. The wavefunction Ψ is the *total* wavefunction for a collection of atoms, or an atomic system, describing both the nuclei and their electrons simultaneously. The Hamiltonian can be divided into several constituent parts,

$$\mathcal{H} = \mathcal{T}_{\text{n}} + \mathcal{T}_{\text{e}} + V_{\text{ne}} + V_{\text{ee}} + V_{\text{nn}} \tag{4.2}$$

where the first two terms describe the kinetic energy of the nuclei and electrons, and the last three terms describe the pair-wise Coulombic nucleus-electron, electron-electron,

and nucleus-nucleus interactions. V_{ne} is often called the external potential and instead labelled V_{ext}, which then includes the effects of external electric and magnetic fields if present. The Schrödinger equation encodes all information about an atomic system, and any property can in principle be deduced from its solution. The problem is thus highly interesting to chemists and materials scientists. Unfortunately, solving it for anything beyond very simple molecules is extremely challenging.

To make the problem slightly more tractable, the Born-Oppenheimer approximation is invoked. [81] An electron is more than three orders of magnitude lighter than even the lightest nucleus, so a reasonable approximation is to consider the nuclei to be *infinitely* heavy. $\mathcal{T}_{\text{n}}$ is neglected and the electrons can be considered to be moving in a field of fixed nuclei. This allows for the splitting of electronic and nucleic degrees of freedom in Eq. (4.1), resulting in an electronic Hamiltonian,

$$\mathcal{H}_{\text{e}} = \mathcal{T}_{\text{e}} + V_{\text{e}} + V_{\text{ee}}, \tag{4.3}$$

as well as a corresponding Schrödinger equation,

$$\mathcal{H}_{\text{e}}\Psi_{\text{e}} = E_{\text{e}}\Psi_{\text{e}}, \tag{4.4}$$

with wavefunctions Ψ_{e} and energy eigenvalues E_{e}. Within the Born-Oppenheimer approximation, nuclei are considered to be moving on the potential energy surface (PES) generated by the solution of Eq. (4.4), giving access to their dynamics. This in principle allows for the structural optimization of atomic structures by displacing nuclei along the gradient of the PES, but the solution of Eq. (4.4), unfortunately, remains challenging despite the simplification made here. Many approximations to the electronic Schrödinger equations have been developed, several of which are routinely used in computational chemistry and materials science.

4.2 Density functional theory

One of the most widespread methods for solving the electronic Schrödinger equation is based on density functional theory (DFT), primarily due to the balance it strikes between accuracy and computational cost. This is accomplished through the Hohenberg-Kohn (HK) theorems, which show that the ground-state energy of any atomic system is a functional of the ground-state density. [82] In short, the first theorem states that the external potential V_{ext}, essentially V_{ne} of Eq. (4.3), is a unique functional of the electron density. The second states that the ground-state density $n_0(\mathbf{r})$ minimizes the energy of the system, which in turn is a functional of the density. The second theorem is often formulated as a variational principle, i.e.,

$$\left.\frac{\partial E[n(\mathbf{r})]}{\partial n(\mathbf{r})}\right|_{n_0} = 0. \tag{4.5}$$

Two things are important to note here. First, the theorems are valid only for the ground-state energy and density. Second, the theorems are by themselves not sufficient to *calculate* the ground-state density, as the energy functional is unknown. It is possible to formulate approximations of it, however, and early attempts to do so include the Thomas-Fermi approach to DFT, which predates the HK theorems by several decades. Formulations of DFT that attempt to construct a fully density-based approach to solving the problem are called *orbital-free*, but none have offered sufficient accuracy to reach widespread use.

Instead, modern implementations are based on the Kohn-Sham (KS) formulation of DFT. [83] The key obstacle is the presence of many-body interactions, which KS theory abstracts away by considering an auxiliary system of non-interacting single-electron states described by wavefunctions, or orbitals, $\psi_i(\mathbf{r})$ which relate to the electronic density $n(\mathbf{r})$ through

$$n(\mathbf{r}) = \sum_{i=1}^{N} |\psi_i(\mathbf{r})|^2. \tag{4.6}$$

By requiring these orbitals to be orthonormal and invoking the HK variational principle one ends up with the Schrödinger-like KS equations,

$$\left(\mathcal{T}_s + V_{\text{ext}}(\mathbf{r}) + V_{\text{H}}(\mathbf{r}) + V_{\text{xc}}(\mathbf{r})\right)\psi_i(\mathbf{r}) = \varepsilon_i \psi_i(\mathbf{r}), \tag{4.7}$$

where $\mathcal{T}_s$ is the kinetic energy of the KS single-particle states, V_{H} the Hartree potential which describes the Coulomb interaction between electrons within a mean-field approximation, V_{ext} the external potential arising from the nuclei,[1] and V_{xc} the exchange-correlation (XC) potential. The corresponding total energy functional is then

$$E_{\text{tot}}[n] = E_{\text{kin}}[n] + E_{\text{H}}[n] + E_{\text{ext}}[n] + E_{\text{xc}}[n]. \tag{4.8}$$

The problematic many-body effects, i.e., electronic exchange and correlation, are bundled into the XC term. The theoretical foundations of KS DFT are exact, but the XC potential has no known analytic form. Approximations must be made to solve the equations in practice.

4.2.1 Exchange-correlation functionals

While the exact form of the XC potential V_{xc}, or equivalently the XC energy functional E_{xc}, is unknown, many of its properties and asymptotic behaviours are known. These can be used to find workable approximations. Their accuracy and predictive power depend on the system under study and the properties of interest, but many have nevertheless turned out to be useful. For spin-polarized systems, the approximations are functionals of *both* spin densities; this detail is omitted here.

[1] V_{ext} also includes external magnetic or electric fields, if they are present.

Local Density Approximation

The simplest XC functional assumes that the electron density behaves as in the homogeneous electron gas, for which the exchange and correlation energies are known to a very high degree of precision. This assumption defines the local density approximation (LDA) and yields a functional depending only on the density at a point, [84]

$$E_{\mathrm{xc}}^{\mathrm{LDA}}[n(\mathbf{r})] = \int \mathrm{d}\mathbf{r}\; n(\mathbf{r})\; \varepsilon_{\mathrm{xc}}^{\mathrm{hom}}\left(n(\mathbf{r})\right), \tag{4.9}$$

where $\varepsilon_{\mathrm{xc}}^{\mathrm{hom}}$ is the XC energy per particle of a homogeneous electron gas. While the behaviour of electrons in real materials differs from this description, the LDA is reasonable for systems where the density varies slowly. The functional generally exaggerates bond strengths in molecular systems, resulting in overestimated atomization energies and underestimated bond lengths.

Generalized Gradient Approximation

Improving upon the LDA involves considering an inhomogeneous electron gas. In the generalized gradient approximation (GGA), this is done by incorporating the density's gradient, $\nabla n(\mathbf{r})$, in addition to the density itself: [84]

$$E_{\mathrm{xc}}^{\mathrm{GGA}}[n(\mathbf{r})] = \int \mathrm{d}\mathbf{r}\; f\left[n(\mathbf{r}), \nabla n(\mathbf{r})\right]. \tag{4.10}$$

Many parametrizations have been developed, with varying popularity and usefulness. The fully non-empirical Perdew-Burke-Ernzerhof (PBE) functional [85] is one of the more popular choices, [86] especially within the solid state community. [87]

Hybrid Density Functionals

While GGA functionals improve upon the LDA in many aspects, they still severely underestimate bandgaps and tend to overstabilize delocalized charge states. [88–90] Unlike the exact XC description, semilocal[2] GGA functionals exhibit self-interaction, i.e., the spurious interaction of each electron with its own charge density. Correcting this self-interaction error (SIE) allows for better bandgap predictions and a proper description of charge localization in e.g. polarons. [91, 92] One way to accomplish this is to employ a hybrid functional, where a semilocal description of exchange and correlation is combined with the fully non-local Hartree-Fock (HF) exchange energy, which counteracts self-interaction. Its inclusion thus reduces the magnitude of SIE in the resulting XC description. The exact manner in which these functionals are constructed varies, however, and the optimal fraction of HF exchange is dependent both on the system

[2] XC functionals of the density and its derivatives.

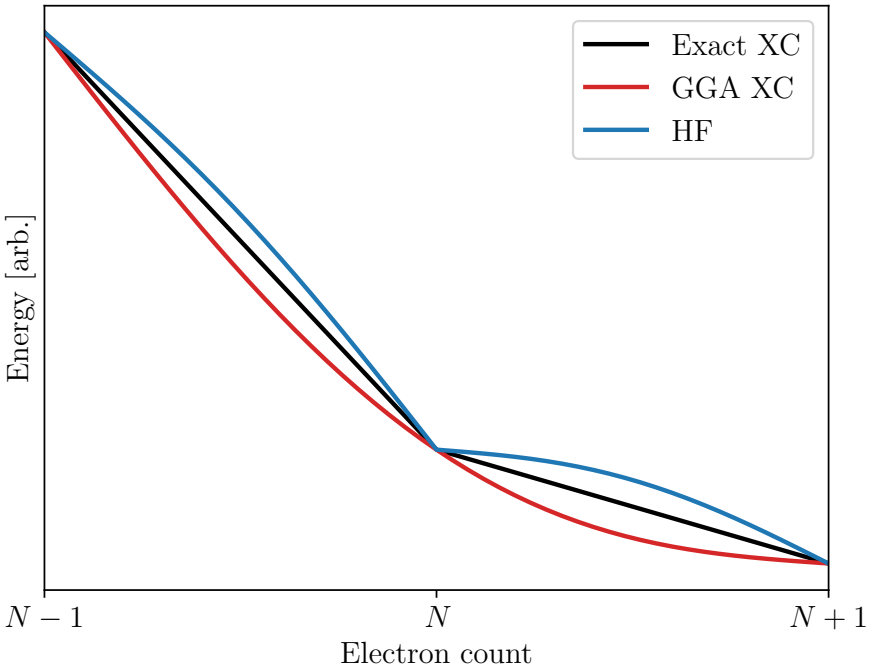

Figure 4.1: A schematic illustration of energy as a function of electron number for fractional charges. The behaviour of the exact XC functional is shown in black, typical GGA behaviour in red, and HF theory in blue.

under study and the properties of interest. [93, 94] One of the more popular variants of hybrid functionals is PBE0, which is simply the PBE functional with a fraction of its exchange description replaced with that of HF theory. [94, 95]

The issues with GGA functionals can also be understood through another quantitative difference in how these approximations behave in comparison to the exact XC energy, which is known to be piecewise linear, i.e., exhibiting a straight-line behaviour for fractional charges. [89, 96, 97] GGA functionals instead tend to exhibit convex behaviour, while the HF is concave as illustrated in Fig. 4.1. A properly designed hybrid functional can approximately recover piecewise linearity, and thereby alleviate the aforementioned problems with semilocal functionals. [98]

4.3 Hartree-Fock method

Unlike DFT, the HF method does not consider an auxiliary system of non-interacting electrons. Instead, the total N-electron wavefunction $\Psi(\{\mathbf{r}\})$ is expressed as a Slater

determinant of single-particle states $\{\psi_i\}$:

$$\Psi(\{\mathbf{r}\}) = \frac{1}{\sqrt{N!}} \begin{vmatrix} \psi_1(\mathbf{r}_1) & \psi_2(\mathbf{r}_1) & \dots & \psi_N(\mathbf{r}_1) \\ \psi_1(\mathbf{r}_2) & \psi_2(\mathbf{r}_2) & \dots & \psi_N(\mathbf{r}_2) \\ \vdots & \vdots & & \vdots \\ \psi_1(\mathbf{r}_N) & \psi_2(\mathbf{r}_N) & \dots & \psi_N(\mathbf{r}_N) \end{vmatrix}. \tag{4.11}$$

Writing the wavefunction in this manner ensures that the Pauli exclusion principle is fulfilled, i.e., no two electrons can occupy the same state. By invoking a variational principle and requiring the single-particle states to be orthonormal it is possible to derive the HF equations,

$$\left(\mathcal{T}_s + V_{\text{ext}}(\mathbf{r}) + V_{\text{H}}(\mathbf{r})\right)\psi_i(\mathbf{r}) + \int \mathrm{d}\mathbf{r}'\; V_{\text{x}}(\mathbf{r},\mathbf{r}')\psi_i(\mathbf{r}') = \varepsilon_i\psi_i(\mathbf{r}), \tag{4.12}$$

which bear a striking resemblance to the KS equations in Eq. (4.7), replacing the XC potential with the fully nonlocal exchange potential V_{x}. HF theory lacks any description of correlation beyond that which is included in the mean-field Coulomb interaction of V_{H}, however, which severely limits its accuracy in many applications.

4.4 Practical considerations

4.4.1 Extended systems and the supercell method

Periodic boundary conditions are typically employed in studies of condensed matter. This allows for the study of crystalline materials, i.e., extended systems, without direct consideration all of the 10^{10} atoms contained even in small crystallites. The idea is illustrated in Fig. 4.2a for a two dimensions; only a single unit cell is explicitly included in the model, while those surrounding it are implicitly included through periodicity. Here, the unit cell includes only a single atom, which makes a proper description of phenomena such as thermal motion or defect formation impossible. This can be circumvented by explicitly including several unit cells in the simulation. Such a construction is called a supercell and is illustrated in Fig. 4.2b. The number of unit cells necessary in its construction depends on the system under study and the phenomena that are of interest; thermally induced disorder may require a few hundred atoms to be included, while a few unit cells may be enough for simpler lattice vibrations. The supercell method can also be used to approximate wholly disordered systems, such as liquids, so long as it is taken to be sufficiently large.

4.4.2 Basis sets

The KS wavefunctions, i.e., solutions to Eq. (4.7), are continuous functions of unknown form whose representation is nontrivial. It is possible to employ real-space grid-based

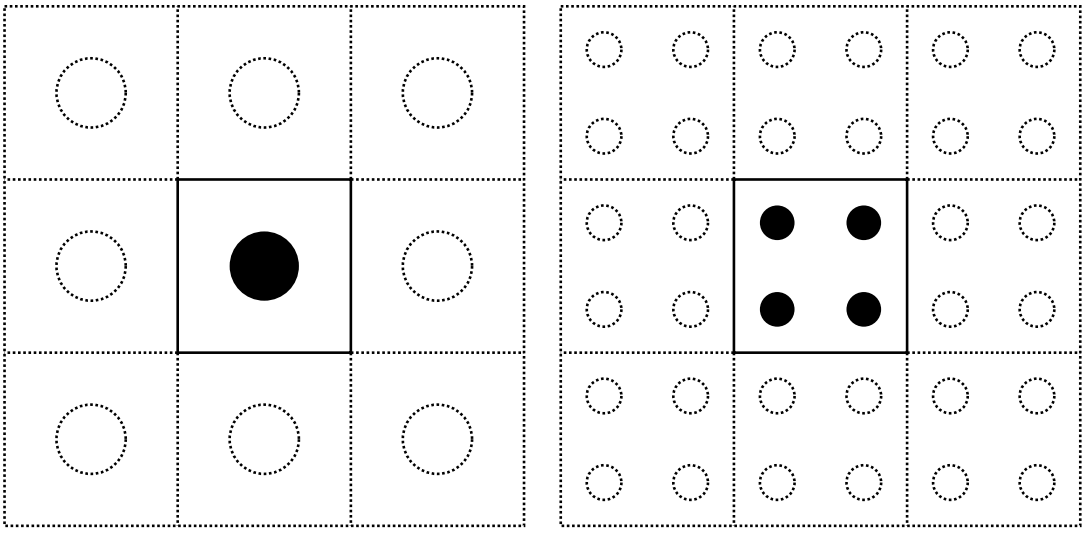

(a) Unit cell. **(b)** Supercell.

Figure 4.2: Schematic illustrations of periodic boundary conditions for a 2D a) unit cell and b) supercell. Filled circles represent explicitly included atoms, and dashed ones represent their periodic images.

approaches, where the wavefunctions are defined at discrete points in space, but such methods tend to be prohibitively expensive. Instead, the wavefunctions are commonly represented in therms of a basis set expansion of the form

$$\psi_i(\mathbf{r}) = \sum_j c_{ji}\phi_j(\mathbf{r}), \tag{4.13}$$

where c_{ji} are expansion coefficients corresponding to the basis functions ϕ_j. Solving the KS equations then becomes a question of finding the set of expansion coefficients. Eq. (4.13) is exact in the limit of basis set completeness, which requires an infinite set of basis functions. This is clearly impractical, so the expansion is typically truncated at a point where errors become negligible while maintaining computational feasibility.

The basis functions ϕ_j can be chosen in numerous ways, each with its own benefits and drawbacks. Two of the most common ones, and the ones used in the calculations performed as part of this thesis, are plane waves and Gaussians.

Plane waves

Using a plane wave basis, the KS wavefunctions may be expressed as

$$\psi_j(\mathbf{r}) = \sum_{\mathbf{G}} c_j(\mathbf{G})e^{i\mathbf{G}\cdot\mathbf{r}}, \tag{4.14}$$

where i denotes the imaginary unit and $\mathbf{G}$ a reciprocal lattice vector.[3] In practice, this infinite Fourier series must be truncated at some point. This is typically done by specifying a cutoff energy, which defines the largest $\mathbf{G}$ included in the expansion through the relation

$$E_{\text{cut}} = \frac{|\mathbf{G}_{\text{max}}|^2}{2}. \tag{4.15}$$

The basis set may thus be systematically improved by increasing E_{cut}, if necessary. This representation is commonly employed in studies of condensed matter, as its natural periodicity complements the periodic boundary conditions commonly employed to model extended systems. A drawback of using plane waves is their delocalized nature; the requisite size of the basis set to reach a given computational accuracy scales with the size of the system, even if large parts of it consists of vacuum.

Gaussians

Using a Gaussian basis set, or set of a Gaussian-type orbitals, the KS wavefunctions may be expressed in polar coordinates as

$$\psi_i(r, \theta, \gamma) = \sum_{(nlm)} c_{i,(nlm)} N Y_{l,m}(\theta, \varphi) r^{2n-2-l} e^{-\zeta r^2}, \tag{4.16}$$

where N is a normalization constant, $Y_{l,m}$ are spherical harmonic functions, and n, l as well as ζ are shape-determining constants. Gaussian-type orbitals are localized and typically atom-centered. The requisite basis set size does not scale with the size of the system, only with the number and type of atoms considered; including vacuum regions does not incur a significant increase in computational cost. A great advantage of this representation is that it allows for the analytical solution of some integrals appearing in the KS and HF equations, making them computationally efficient. Unlike plane waves, there is no systematic way of improving the quality of a Gaussian basis set. Instead, they must be designed and optimized to minimize errors on a set of reference structures, the choices of which may limit the transferability of the resulting representation.

4.4.3 Pseudopotential approximation

Typical systems of interest to materials science may contain thousands of electrons, but only the valence states meaningfully respond to changes in the chemical environment. The core states hardly participate in bonding and thus do not need to be treated with the same level of detail; the potential arising from the nuclei and core electrons are thus commonly bundled into a pseudopotential, simplifying their description. This can be done in such a way that the resulting valence pseudo-wavefunctions are smooth inside

[3] Discussion of reciprocal space in general is left out of this thesis for brevity.

of some cutoff radius R_{cut}, and in agreement with the all-electron result outside; this is illustrated in Fig. 4.3. As a consequence, the number of states explicitly included in the KS equations is reduced significantly, and their pseudo-wavefunctions may be represented using fewer basis functions than in the all-electron case. This constitutes a significant reduction in computational complexity while retaining a high level of accuracy. Precisely which states should be included in the pseudopotential is not clear-cut, since the core-valence division is approximative in nature, but typically includes at least the outermost shell of the atomic electronic structure for each element. There is also some freedom in how to choose the behaviour of the potential within R_{cut}. A common choice is to enforce that the norm of each pseudo-wavefunction is equal to the norm of the corresponding all-electron wavefunction, resulting in the class of norm-conserving pseudopotentials.

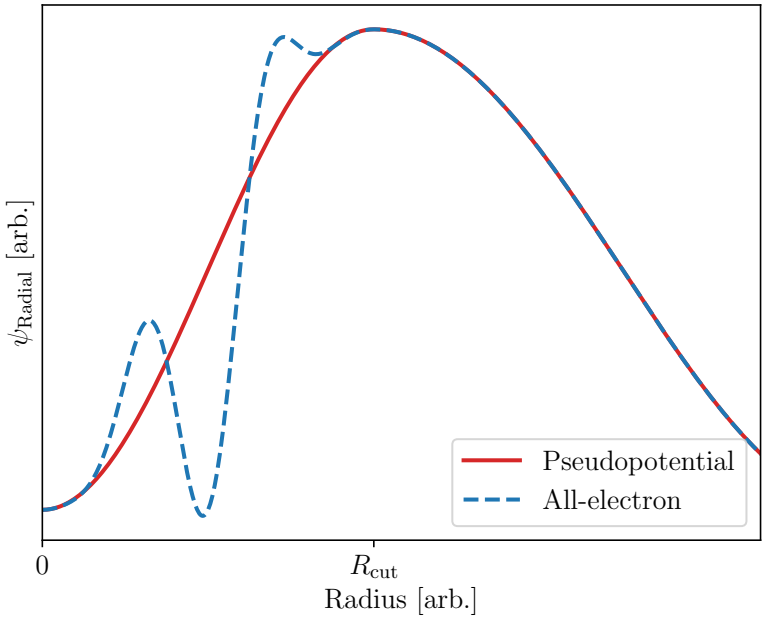

Figure 4.3: Sketch of radial wavefunctions ψ_{Radial} with the use of pseudopotentials (solid red) and without (dashed blue).

4.4.4 Solving the Kohn-Sham equations

Solving the KS equations can be done using standard computational techniques for eigenvalue problems, but one first has to construct the effective potential,

$$V_{\text{eff}}(\mathbf{r}) = V_{\text{H}}(\mathbf{r}) + V_{\text{ext}}(\mathbf{r}) + V_{\text{XC}}(\mathbf{r}).$$

The Hartree and XC potentials depend on the electronic density, however, which is determined using the KS wavefunctions. This means that a self-consistent scheme needs

to be applied. Such a scheme is illustrated in Fig. 4.4; the initial density can be generated e.g. completely randomly, or using a linear combination of hydrogen-like atomic orbitals.

In short, the initial density is used to solve Eq. (4.7) for the set of KS wavefunctions. These are then used to compute a new density. If the new density agrees with the initial one, within some threshold, the procedure is considered to be converged. Otherwise, the procedure is restarted using the updated density and repeated until convergence is reached.

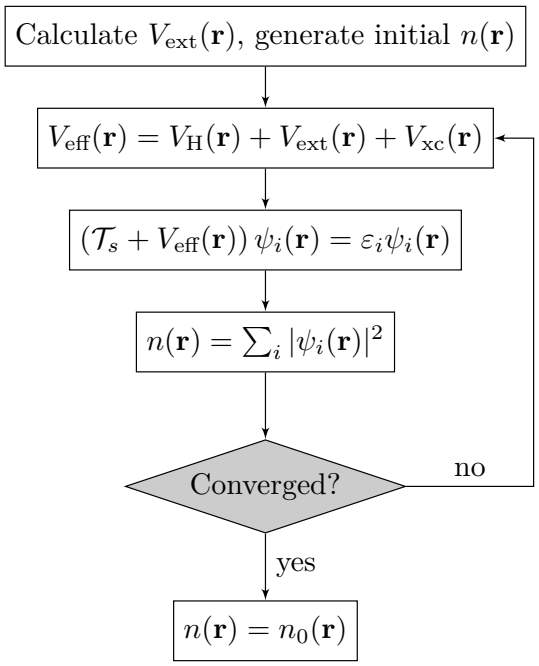

Figure 4.4: A self-consistent scheme for solving the KS equations.

4.4.5 CP2K

The choice of DFT software is less important than in the past, as accurate results are achievable with the majority of options, [99] but the capabilities still differ somewhat between them. This thesis relies on hybrid-functional DFT calculations, which are significantly more computationally demanding than those performed at the GGA level of theory; the software used for these computations, CP2K, implements several techniques that reduces the effort required in evaluating the HF exchange contribution to the total energy, [100] making the use of larger supercells feasible. This is especially important in the study of defects, where the dilute limit is typically of interest. In the following, a short introduction is given to some of these methods.

Gaussian and Plane Wave Method

As previously discussed, the choice of basis set is associated with both advantages and disadvantages. However, it is in principle possible to combine different basis sets, and thus circumvent some of the drawbacks associated with the choice. CP2K implements the Gaussian and Plane Waves (GPW) method, which makes use of a primary set of Gaussian-type orbitals for the KS wavefunctions along with an auxiliary planewave basis set for the density. [101, 102]

With Gaussian-type orbitals, the terms of the KS total energy in Eq. (4.8) can be expressed in terms of a density matrix **P** with elements

$$P^{\mu\nu} = \sum_i c_{\mu i} c_{\nu i}, \tag{4.17}$$

where $c_{\mu i}$ and $c_{\nu i}$ are the basis set expansion coefficients of Eq. (4.13). In this representation, the evaluation of the Hartree and XC potentials are the computational bottlenecks, while the kinetic energy and external potentials may be evaluated efficiently. By expanding the electronic density into a set of planewaves, $n_{\mathrm{PW}}(\mathbf{r}) \approx n(\mathbf{r})$, efficient Fourier-space approaches can be utilized for those terms instead. The GPW KS energy functional can then be expressed as

$$E[\mathbf{P}] = E_{\mathrm{kin}}[\mathbf{P}] + E_{\mathrm{ext}}[\mathbf{P}] + E_{\mathrm{H}}[n_{\mathrm{PW}}] + E_{\mathrm{xc}}[n_{\mathrm{PW}}], \tag{4.18}$$

thus making use of the advantages of both basis sets.

PBE0-TC-LRC

The hybrid functional used for the calculations in this thesis is a modified version of PBE0. [94, 95] Its exchange energy may be expressed as

$$E_{\mathrm{x}}^{\mathrm{PBE0}} = \alpha E_{\mathrm{x}}^{\mathrm{HFX}} + (1-\alpha) E_{\mathrm{x}}^{\mathrm{PBE}}, \tag{4.19}$$

where α denotes the fraction of HF exchange $E_{\mathrm{x}}^{\mathrm{HFX}}$ to be mixed in with the PBE exchange energy $E_{\mathrm{x}}^{\mathrm{PBE}}$. This expression is difficult to compute under periodic boundary conditions, however, thanks to the presence of a singularity in the Coulombic HF interaction potential; this issue can be circumvented by truncating this interaction, setting it to 0 outside of a cutoff radius R_C. [103, 104] The resulting truncated Coulomb-variant of the functional, PBE0-TC, is significantly easier to evaluate than the full PBE0 description while retaining high accuracy. The exchange energy typically converges sufficiently fast for this to be a useful approximation, but the convergence behaviour can be improved further by correcting for the missing exchange description beyond R_C. The long-range corrected truncated-Coulomb exchange functional PBE0-TC-LRC can thus be constructed as [104]

$$E_{\mathrm{x}}^{\mathrm{PBE0\text{-}TC\text{-}LRC}} = \alpha E_{\mathrm{x}}^{\mathrm{HFX,TC}} + \alpha E_{\mathrm{x}}^{\mathrm{PBE,LRC}} + (1-\alpha) E_{\mathrm{x}}^{\mathrm{PBE}}, \tag{4.20}$$

where $E_{\mathrm{x}}^{\mathrm{HFX,TC}}$ is the truncated-Coulomb description of the HF exchange energy, and $E_{\mathrm{x}}^{\mathrm{PBE,LRC}}$ the corresponding long-range corrections computed at the PBE level of theory.

Auxilliary Density Matrix Method

The computational bottleneck in hybrid DFT lies in the evaluation of the HF exchange energy. Using density matrix notation, this energy may be expressed as

$$E_{\mathrm{x}}^{\mathrm{HFX}} = -\frac{1}{2}\sum_{\lambda\sigma\mu\nu} P^{\mu\sigma}P^{\nu\lambda}\int \mathrm{d}\mathbf{r}\int \mathrm{d}\mathbf{r}'\phi_\mu(\mathbf{r})\phi_\nu(\mathbf{r})g(\mathbf{r},\mathbf{r}')\phi_\lambda(\mathbf{r}')\phi_\sigma(\mathbf{r}'), \tag{4.21}$$

where the density matrix elements P^{ij} are defined according to Eq. (4.17) and ϕ_i are the corresponding Gaussian basis functions. This limits the system size feasibly accessible using the method, but it can be extended significantly by using the Auxiliary Density Matrix Method (ADMM). [105] By introducing an auxiliary basis set with corresponding density matrix $\hat{\mathbf{P}}$, chosen to be smaller than the primary basis set, the HF exchange energy $E_{\mathrm{X}}^{\mathrm{HFX}}$ may approximated as

$$E_{\mathrm{X}}^{\mathrm{HFX}}[\mathbf{P}] = E_{\mathrm{X}}^{\mathrm{HFX}}[\hat{\mathbf{P}}] + E_{\mathrm{X}}^{\mathrm{HFX}}[\mathbf{P}] - E_{\mathrm{X}}^{\mathrm{HFX}}[\hat{\mathbf{P}}] \tag{4.22}$$

$$\approx E_{\mathrm{X}}^{\mathrm{HFX}}[\hat{\mathbf{P}}] + E_{\mathrm{X}}^{\mathrm{DFT}}[\mathbf{P}] - E_{\mathrm{X}}^{\mathrm{DFT}}[\hat{\mathbf{P}}]. \tag{4.23}$$

This significantly reduces the number of terms in Eq. (4.21), since $E_{\mathrm{X}}^{\mathrm{HFX}}$ only needs to be calculated using $\hat{\mathbf{P}}$ rather than the full-size $\mathbf{P}$.

5

Defect modelling

5.1 Defect formation energies

Defects within a host material can be treated in the same way as pristine materials, for instance using the supercell method within DFT. The total energies of two different defects within a host material are not directly comparable, however, as they contain a different number of atoms. To estimate and compare their relative stabilities one can make use of the formation energy of a defect X in charge state q, which may be defined as [106, 107]

$$E^f[X^q] = E[X^q] - E[\text{host}] - \sum_i n_i \mu_i + q\left(\varepsilon_F - \varepsilon_v - \Delta V_{0/b}\right) + E_{\text{corr}}, \tag{5.1}$$

where $E[X^q]$ is the total energy of the defective supercell, $E[\text{host}]$ the total energy of the host material, μ_i the chemical potentials of the n_i added ($n_i > 0$) or removed ($n_i < 0$) defect atoms, ε_F the Fermi energy, ε_v the VBM, and $\Delta V_{0/b}$ a term that aligns the electrostatic potential of the defect supercell with that of the host. Finally, E_{corr} is an *a posteriori* correction term accounting for finite-size effects stemming from spurious interactions between periodic repetitions of the defect in the supercell approach. Typically, the defect behaviour at the dilute limit is of interest, i.e., at defect concentrations low enough to make defect-defect interactions negligible. While some of these unwanted contributions shrink reasonably fast with increasing supercell sizes, such as elastic energies arising from lattice relaxation, others decrease much slower — notably, the electrostatic interaction between image charges of defect systems with $q \neq 0$ persist over longer distances. [108] As such, these spurious electrostatic interactions are often corrected for. This is discussed in some more detail in the next section.

The Fermi energy ε_F, i.e., the chemical potential of electrons, is not fixed and is typically plotted against. Similarly, the chemical potentials μ_i, are treated as variables and

can be chosen to mimic different synthesis conditions. These choices are constrained, however, as the chemical potentials are subject to thermodynamic limitations. This is best illustrated using an example, where the approach of Freysold *et al.* [107] is adopted, neglecting the effects of finite temperature and pressure. Under equilibrium growth of $BiVO_4$, the chemical potentials are subject to the constraint

$$\mu_{\mathrm{Bi}} + \mu_{\mathrm{V}} + 4\mu_{\mathrm{O}} = E(\mathrm{BiVO_4}) \tag{5.2}$$

to ensure the stability of $BiVO_4$. Here, $E(\mathrm{BiVO_4})$ is the DFT total energy of $BiVO_4$ per formula unit. Eq. (5.2) is dependent on the choice of reference systems for the constituent atoms, however. This can be circumvented by rewriting this condition in terms of the formation enthalpy instead, which may be expressed as

$$\Delta H_f(\mathrm{BiVO_4}) = E(\mathrm{BiVO_4}) - \mu_{\mathrm{Bi}}^{\mathrm{ref}} - \mu_{\mathrm{V}}^{\mathrm{ref}} - 4\mu_{\mathrm{O}}^{\mathrm{ref}}, \tag{5.3}$$

where μ_i^{ref} is the chemical potential of species i with respect to some choice of reference reservoir. Here, an appropriate choice is the DFT energies per atom of bulk vanadium and bismuth metal, as well as an oxygen molecule. Combining Eq. (5.2) and Eq. (5.3) yields

$$\begin{aligned} \Delta H_f(\mathrm{BiVO_4}) &= (\mu_{\mathrm{Bi}} - \mu_{\mathrm{Bi}}^{\mathrm{ref}}) + (\mu_{\mathrm{V}} - \mu_{\mathrm{V}}^{\mathrm{ref}}) + 4(\mu_{\mathrm{O}} - E_{\mathrm{O}}^{\mathrm{ref}}) && (5.4)\\ &= \Delta\mu_{\mathrm{Bi}} + \Delta\mu_{\mathrm{V}} + 4\Delta\mu_{\mathrm{O}}, && (5.5) \end{aligned}$$

where each $\Delta\mu$ is independent of reference choices. Upper bounds for these quantities may be found by preventing the formation of bulk metal and gaseous oxygen, imposing the constraints

$$\Delta\mu_{\mathrm{Bi}} \leq 0, \quad \Delta\mu_{\mathrm{V}} \leq 0, \quad \Delta\mu_{\mathrm{O}} \leq 0. \tag{5.6}$$

$BiVO_4$ is not the only oxide that could form during synthesis, however, and it is desirable to suppress the formation of secondary products. This subjects each $\Delta\mu$ to further constraints. Considering the formation of VO_2, V_2O_5, and Bi_2O_3 gives that

$$\begin{aligned} \Delta H_f(\mathrm{VO_2}) &\geq \Delta\mu_{\mathrm{V}} + 2\Delta\mu_{\mathrm{O}}, && (5.7)\\ \Delta H_f(\mathrm{V_2O_5}) &\geq 2\Delta\mu_{\mathrm{V}} + 5\Delta\mu_{\mathrm{O}}, && (5.8)\\ \Delta H_f(\mathrm{Bi_2O_3}) &\geq 2\Delta\mu_{\mathrm{Bi}} + 3\Delta\mu_{\mathrm{O}}, && (5.9) \end{aligned}$$

ensuring that $BiVO_4$ is the only stable product.

The constraints of Eqs. (5.5)–(5.9) can be visualized in the form of a phase diagram, as shown in Fig. 5.1, where the upper bounds represent Eq. (5.6) and the lower bounds Eq. (5.5). The lines within the boundaries represent Eq. (5.9); the region where all these constraints are fulfilled, and $BiVO_4$ formation thus favorable, is represented by shading. The defect formation energies for the native defects of $BiVO_4$ at the chemical potentials marked by red dots in Fig. 5.1 are shown in Fig. 5.2. In **Paper II**, the stability of the native defects of $BiVO_4$ is investigated using the method outlined above.

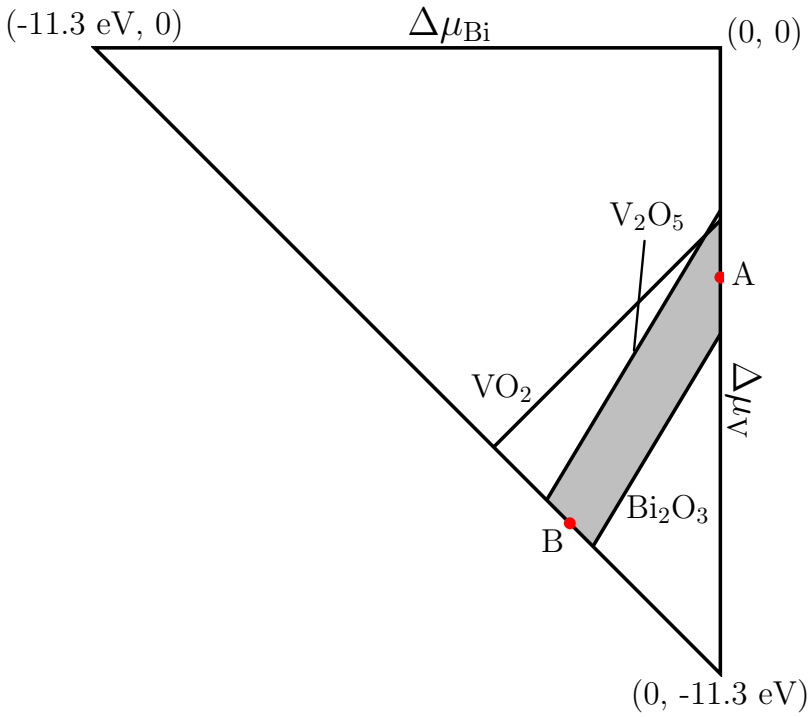

Figure 5.1: Phase diagram of $BiVO_4$ formation with competing side reactions. The region of stability, i.e., where Eqs. (5.5)–(5.9) are fulfilled, for $BiVO_4$ is shaded in grey. Based on data from **Paper II**. [65]

5.2 Charged defects

The term E_{corr} in Eq. (5.1) demands special attention. While modelling the effects of e.g. spurious wavefunction overlap and elastic interactions is possible, [107] it is commonplace to correct only for electrostatic interactions arising for charged defects. This is typically done using an *ad hoc* correction scheme.

The simplest such scheme uses the Madelung energy, which describes the energy of a point charge array with neutralizing background, [109]

$$E_{\mathrm{corr}}^{\mathrm{Madelung}} = \frac{q^2\alpha}{2L}, \tag{5.10}$$

where α is the Madelung constant, dependent on the Bravais lattice of the defect's host crystal, and L is a typical supercell dimension. Real defects cannot always be described as point charges, however, in which case this description is insufficient.

In this sense, the scheme of Freysoldt, Neugebauer and Van de Walle is more adaptable. [110, 111] A model charge distribution is chosen, and the electrostatics of the

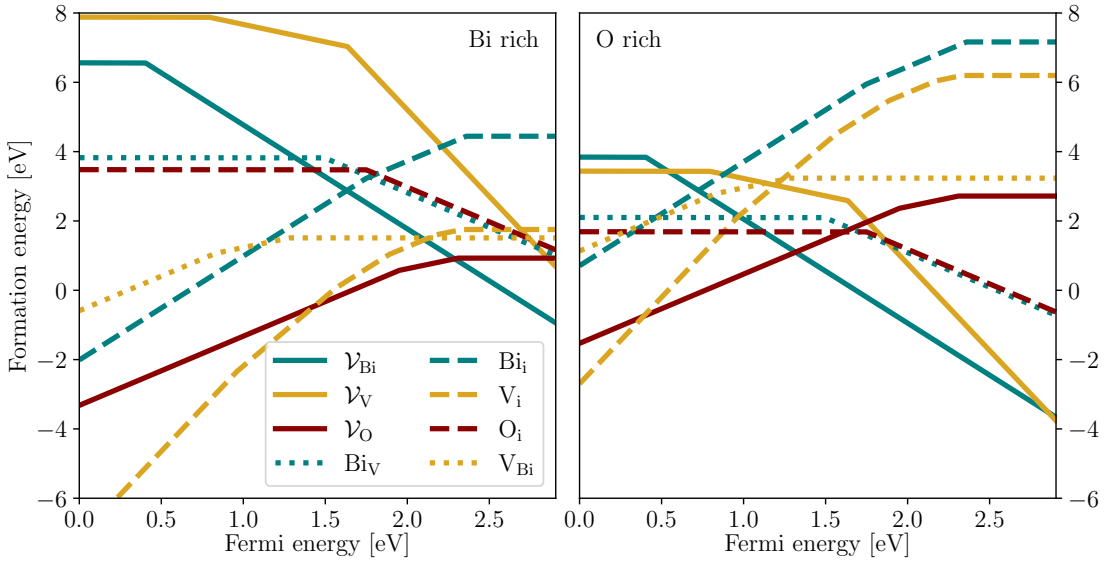

Figure 5.2: Defect formation energies for the native defects of $BiVO_4$. A vacancy of species A is denoted $\mathcal{V}_A$, an A interstitial A_i, and a substitutional A atom on a B site A_B. Based on data from **Paper II**. [65]

defect is estimated based on this model. The correction term is then given by

$$E_{corr}^{FNV} = E_{lat} - q\Delta V_{q/0}, \tag{5.11}$$

where E_{lat} is the difference in electrostatic energy between isolated and periodic model charge densities, q the defective system's charge, and $qV_{q/0}$ a term that aligns the electrostatic potentials of the charged and neutral defect supercells. This scheme is widely used and has been found to produce robust and consistent results; [106] in **Paper II**, we make use of the method to study the native defects in $BiVO_4$ in different charge states.

6

Summary of papers

Paper I

Influence of Oxygen Vacancies on the structure of $BiVO_4$

In **Paper I**, oxygen vacancies in tetragonal scheelite bismuth vanadate are studied. A thorough search for stable configurations in the host material is undertaken, and these structures are then subjected to variable-cell optimization, allowing the lattice parameters to change along with the atomic positions. The presence of the vacancy induces significant lattice distortions, which grow more pronounced with increased defect concentration. These distortions persist at finite temperatures.

To get insight into how oxygen deficiency might affect experimental characterization of $BiVO_4$ samples, we simulate the powder X-ray diffraction patterns of the distorted defective as well as the pristine tetragonal and monoclinic scheelite structures. We find that the distortions induce splitting of diffraction peaks bearing a strong resemblance to that of monoclinic $BiVO_4$. This splitting is clear at experimentally achievable oxygen vacancy concentrations, but becomes more pronounced as it increases.

The computed diffraction patterns are finally compared to some examples from experimental literature. The experimental results vary in quality, which renders their interpretation somewhat ambiguous, and all three patterns bear stronger resemblance to those of the oxygen-deficient structures than that of pristine *ms* $BiVO_4$. This suggests that X-ray diffraction may be insufficient to unambiguously verify that monoclinic bismuth vanadate has been synthesized, and complementary characterization techniques should be employed to rule out significant oxygen deficiency.

Paper II

Charge Localization in Defective $BiVO_4$

In **Paper II**, the native defects of bismuth vanadate are studied in the material's monoclinic scheelite phase. As excess charges tend to localize in the material, a thorough investigation of the relative stability of different polaronic configurations around each defect is conducted. We find that charge localization greatly affects the lattice geometry in the vicinity of the defects, and thus plays an important role in the material's defect chemistry. In particular, the excess holes stemming from oxygen interstitials and vanadium vacancies may form bipolarons in the form of oxygen dimers, which have previously been predicted to have an overall positive effect on the water splitting reaction.

Defect formation energies are calculated under different synthesis conditions. Fermi level pinning due to compensation between donors and acceptors leads to p-type conductivity only under a very slim set of oxygen-rich conditions, making it hard to achieve in synthesized samples. Instead, the material exhibits n-type conductivity under a wide range of synthesis conditions. This is in good agreement with experimental literature, where examples of p-type $BiVO_4$ are exceedingly rare.

Our results highlight the complexity of the defect landscape in bismuth vanadate as well as the necessity of taking polaron formation into account in computational studies of defects, both in the $BiVO_4$ and other complex metal oxides, to obtain a full description of defect formation.

7

Outlook

This thesis presents studies of native point defects in the bulk of $BiVO_4$. Near-surface defects at are just as important, however, and their properties cannot be determined by simply extrapolating those in the bulk. Defects that are exposed to electrolyte may furthermore interact with OER intermediates, potentially influencing the reaction barriers. Insight into such effects is of great scientific and technological interest, so extending the discussion of **Paper II** to include surface phenomena is a highly interesting topic.

This holds true for extrinsic defects as well, which were not considered within this thesis. As discussed in Chapter 3, the incorporation of several different impurities has been studied experimentally, to varying degrees of influence on the material's PEC efficiency for the OER. For instance, the incorporation of nitrogen reduces the bandgap of $BiVO_4$, thus allowing for the absorption of a larger part of the visible light spectrum. The overall effect on the OER is unclear, with conflicting reports in the literature. Clarifying the role of the impurity could lead to a reliable doping strategy, or rule out its viability as a dopant.

Acknowledgments

The list of people that have influenced and helped me during my time as a PhD student is too large to put in print. Some people demand special attention, however.

Firstly, I want to thank Julia Wiktor. The work in this thesis would not have been possible without you. Thank you for your guidance and eternal patience!

Secondly, I want to thank Anders Hellman. While your name is absent from my list of coauthors, your influence is what pulled me into academia in the first place. Thank you for believing in me!

Thirdly, I want to thank my coworkers at the division of Condensed Matter and Materials Theory. You make each day at work a little bit brighter. Thank you for that!

Finally, I am grateful that my friends and family still want to be around me. Thanks for putting up with me!

Bibliography

[1] A. Fujishima and K. Honda, *Electrochemical Photolysis of Water at a Semiconductor Electrode,* Nature **238**, 37 (1972). doi:10.1038/238037a0.

[2] A. Kudo, K. Ueda, H. Kato, and I. Mikami, *Photocatalytic O_2 Evolution under Visible Light Irradiation on $BiVO_4$ in Aqueous $AgNO_3$ Solution,* Catalysis Letters **53**, 229 (1998). doi:10.1023/A:1019034728816.

[3] S. D. Tilley, *Recent Advances and Emerging Trends in Photo-Electrochemical Solar Energy Conversion,* Adv. Energy Mater. **9**, 1802877 (2019). doi:10.1002/aenm.201802877.

[4] J. K. Nørskov, J. Rossmeisl, A. Logadottir, L. Lindqvist, J. R. Kitchin, T. Bligaard, and H. Jónsson, *Origin of the Overpotential for Oxygen Reduction at a Fuel-Cell Cathode,* J. Phys. Chem. B **108**, 17886 (2004). doi:10.1021/jp047349j.

[5] I. Chorkendorff and J. W. Niemantsverdriet, *Concepts of Modern Catalysis and Kinetics* (Weinheim: WILEY-VCH Verlag GmbH & Co KG, 2017). ISBN 978-3-527-33268-7.

[6] E. Fabbri and T. J. Schmidt, *Oxygen Evolution Reaction—The Enigma in Water Electrolysis,* ACS Catal. **8**, 9765 (2018). doi:10.1021/acscatal.8b02712.

[7] J. Rossmeisl, A. Logadottir, and J. K. Nørskov, *Electrolysis of Water on (Oxidized) Metal Surfaces,* Chemical Physics **319**, 178 (2005). doi:10.1016/j.chemphys.2005.05.038.

[8] J. Jia, L. C. Seitz, J. D. Benck, Y. Huo, Y. Chen, J. W. D. Ng, T. Bilir, J. S. Harris, and T. F. Jaramillo, *Solar Water Splitting by Photovoltaic-Electrolysis with a Solar-to-Hydrogen Efficiency over 30%,* Nat Commun **7**, 13237 (2016). doi:10.1038/ncomms13237.

[9] M. G. Walter, E. L. Warren, J. R. McKone, S. W. Boettcher, Q. Mi, E. A. Santori, and N. S. Lewis, *Solar Water Splitting Cells,* Chem. Rev. **110**, 6446 (2010). doi:10.1021/cr1002326.

[10] K. T. Fountaine, H. J. Lewerenz, and H. A. Atwater, *Efficiency Limits for Photoelectrochemical Water-Splitting,* Nat Commun **7**, 13706 (2016). doi:10.1038/ncomms13706.

[11] T. Hisatomi, J. Kubota, and K. Domen, *Recent Advances in Semiconductors for Photocatalytic and Photoelectrochemical Water Splitting,* Chem. Soc. Rev. **43**, 7520 (2014). doi:10.1039/C3CS60378D.

[12] C. Ros, T. Andreu, and J. R. Morante, *Photoelectrochemical Water Splitting: A Road from Stable Metal Oxides to Protected Thin Film Solar Cells,* J. Mater. Chem. A **8**, 10625 (2020). doi:10.1039/D0TA02755C.

[13] P. E. de Jongh, D. Vanmaekelbergh, and J. J. Kelly, *Photoelectrochemistry of Electrodeposited Cu_2O,* J. Electrochem. Soc. **147**, 486 (2000). doi:10.1149/1.1393221.

[14] L. Wu, L.-k. Tsui, N. Swami, and G. Zangari, *Photoelectrochemical Stability of Electrodeposited Cu_2O Films,* J. Phys. Chem. C **114**, 11551 (2010). doi:10.1021/jp103437y.

[15] A. Paracchino, V. Laporte, K. Sivula, M. Grätzel, and E. Thimsen, *Highly Active Oxide Photocathode for Photoelectrochemical Water Reduction,* Nature Mater **10**, 456 (2011). doi:10.1038/nmat3017.

[16] L. Pan, J. H. Kim, M. T. Mayer, M.-K. Son, A. Ummadisingu, J. S. Lee, A. Hagfeldt, J. Luo, and M. Grätzel, *Boosting the Performance of Cu_2O Photocathodes for Unassisted Solar Water Splitting Devices,* Nat Catal **1**, 412 (2018). doi:10.1038/s41929-018-0077-6.

[17] M. Ni, M. K. H. Leung, D. Y. C. Leung, and K. Sumathy, *A Review and Recent Developments in Photocatalytic Water-Splitting Using TiO_2 for Hydrogen Production,* Renewable and Sustainable Energy Reviews **11**, 401 (2007). doi:10.1016/j.rser.2005.01.009.

[18] A. Miyoshi, S. Nishioka, and K. Maeda, *Water Splitting on Rutile TiO_2-Based Photocatalysts,* Chem. – Eur. J. **24**, 18204 (2018). doi:10.1002/chem.201800799.

[19] M. Ismael, *A Review and Recent Advances in Solar-to-Hydrogen Energy Conversion Based on Photocatalytic Water Splitting over Doped-TiO_2 Nanoparticles,* Solar Energy **211**, 522 (2020). doi:10.1016/j.solener.2020.09.073.

[20] R. Asahi, T. Morikawa, T. Ohwaki, K. Aoki, and Y. Taga, *Visible-Light Photocatalysis in Nitrogen-Doped Titanium Oxides,* Science **293**, 269 (2001). doi:10.1126/science.1061051.

[21] K. Nukumizu, J. Nunoshige, T. Takata, J. N. Kondo, M. Hara, H. Kobayashi, and K. Domen, *$TiN_xO_yF_z$ as a Stable Photocatalyst for Water Oxidation in Visible Light ($<$570 Nm),* Chem. Lett. **32**, 196 (2003). doi:10.1246/cl.2003.196.

[22] K. Maeda, K. Ishimaki, Y. Tokunaga, D. Lu, and M. Eguchi, *Modification of Wide-Band-Gap Oxide Semiconductors with Cobalt Hydroxide Nanoclusters for Visible-Light Water Oxidation,* Angew. Chem. Int. Ed. **55**, 8309 (2016). doi:10.1002/anie.201602764.

[23] K. Maeda, K. Ishimaki, M. Okazaki, T. Kanazawa, D. Lu, S. Nozawa, H. Kato, and M. Kakihana, *Cobalt Oxide Nanoclusters on Rutile Titania as Bifunctional Units for Water Oxidation Catalysis and Visible Light Absorption: Understanding the Structure–Activity Relationship,* ACS Appl. Mater. Interfaces **9**, 6114 (2017). doi:10.1021/acsami.6b15804.

[24] Y. Park, K. J. McDonald, and K.-S. Choi, *Progress in Bismuth Vanadate Photoanodes for Use in Solar Water Oxidation,* Chem. Soc. Rev. **42**, 2321 (2013). doi:10.1039/C2CS35260E.

[25] H. L. Tan, R. Amal, and Y. H. Ng, *Alternative Strategies in Improving the Photocatalytic and Photoelectrochemical Activities of Visible Light-Driven $BiVO_4$: A Review,* J. Mater. Chem. A **5**, 16498 (2017). doi:10.1039/C7TA04441K.

[26] A. W. Sleight, H. y. Chen, A. Ferretti, and D. E. Cox, *Crystal Growth and Structure of $BiVO_4$,* Mater. Res. Bull. **14**, 1571 (1979). doi:10.1016/0025-5408(72)90227-9.

[27] S. Tokunaga, H. Kato, and A. Kudo, *Selective Preparation of Monoclinic and Tetragonal $BiVO_4$ with Scheelite Structure and Their Photocatalytic Properties,* Chem. Mater. **13**, 4624 (2001). doi:10.1021/cm0103390.

[28] J. K. Cooper, S. Gul, F. M. Toma, L. Chen, P.-A. Glans, J. Guo, J. W. Ager, J. Yano, and I. D. Sharp, *Electronic Structure of Monoclinic $BiVO_4$,* Chem. Mater. **26**, 5365 (2014). doi:10.1021/cm5025074.

[29] B. Lamm, B. J. Trześniewski, H. Döscher, W. A. Smith, and M. Stefik, *Emerging Postsynthetic Improvements of $BiVO_4$ Photoanodes for Solar Water Splitting,* ACS Energy Lett. **3**, 112 (2018). doi:10.1021/acsenergylett.7b00834.

[30] D. K. Zhong, S. Choi, and D. R. Gamelin, *Near-Complete Suppression of Surface Recombination in Solar Photoelectrolysis by "Co-Pi" Catalyst-Modified W:$BiVO_4$,* J. Am. Chem. Soc. **133**, 18370 (2011). doi:10.1021/ja207348x.

[31] F. F. Abdi and R. van de Krol, *Nature and Light Dependence of Bulk Recombination in Co-Pi-Catalyzed $BiVO_4$ Photoanodes,* J. Phys. Chem. C **116**, 9398 (2012). doi:10.1021/jp3007552.

[32] C. Liu, H. Luo, Y. Xu, W. Wang, Q. Liang, N. Mitsuzaki, and Z. Chen, *Cobalt–Phosphate-Modified Mo:$BiVO_4$ Mesoporous Photoelectrodes for Enhanced Photoelectrochemical Water Splitting,* J Mater Sci **54**, 10670 (2019). doi:10.1007/s10853-019-03658-7.

[33] B. J. Trześniewski and W. A. Smith, *Photocharged $BiVO_4$ Photoanodes for Improved Solar Water Splitting,* J. Mater. Chem. A **4**, 2919 (2016). doi:10.1039/C5TA04716A.

[34] M. Favaro, F. F. Abdi, M. Lamers, E. J. Crumlin, Z. Liu, R. van de Krol, and D. E. Starr, *Light-Induced Surface Reactions at the Bismuth Vanadate/Potassium Phosphate Interface,* J. Phys. Chem. B **122**, 801 (2018). doi:10.1021/acs.jpcb.7b06942.

[35] N. J. Firet, A. Venugopal, M. A. Blommaert, C. Cavallari, C. J. Sahle, A. Longo, and W. A. Smith, *Chemisorption of Anionic Species from the Electrolyte Alters the Surface Electronic Structure and Composition of Photocharged $BiVO_4$,* Chem. Mater. **31**, 7453 (2019). doi:10.1021/acs.chemmater.9b02121.

[36] P. Chatchai, Y. Murakami, S.-y. Kishioka, A. Y. Nosaka, and Y. Nosaka, *Efficient Photocatalytic Activity of Water Oxidation over WO_3/$BiVO_4$ Composite under Visible Light Irradiation,* Electrochimica Acta **54**, 1147 (2009). doi:10.1016/j.electacta.2008.08.058.

[37] S. J. Hong, S. Lee, J. S. Jang, and J. S. Lee, *Heterojunction $BiVO_4$/WO_3 Electrodes for Enhanced Photoactivity of Water Oxidation,* Energy Environ. Sci. **4**, 1781 (2011). doi:10.1039/C0EE00743A.

[38] B. S. Kalanoor, H. Seo, and S. S. Kalanur, *Recent Developments in Photoelectrochemical Water-Splitting Using WO_3/$BiVO_4$ Heterojunction Photoanode: A Review,* Materials Science for Energy Technologies **1**, 49 (2018). doi:10.1016/j.mset.2018.03.004.

[39] S. Jessl, J. Rongé, D. Copic, M. A. Jones, J. Martens, and M. D. Volder, *Honeycomb-Shaped Carbon Nanotube Supports for $BiVO_4$ Based Solar Water Splitting,* Nanoscale **11**, 22964 (2019). doi:10.1039/C9NR06737J.

[40] S. Liu, J. Pan, X. Li, X. Meng, H. Yuan, Y. Li, Y. Zhao, D. Wang, J. Ma, S. Zhu, and L. Kong, *In Situ Modification of $BiVO_4$ Nanosheets on Graphene for Boosting Photocatalytic Water Oxidation,* Nanoscale **12**, 14853 (2020). doi:10.1039/D0NR02718A.

[41] B. Pattengale and J. Huang, *The Effect of Mo Doping on the Charge Separation Dynamics and Photocurrent Performance of $BiVO_4$ Photoanodes,* Phys. Chem. Chem. Phys. **18**, 32820 (2016). doi:10.1039/C6CP06407H.

[42] B. Pattengale, J. Ludwig, and J. Huang, *Atomic Insight into the W-Doping Effect on Carrier Dynamics and Photoelectrochemical Properties of $BiVO_4$ Photoanodes,* J. Phys. Chem. C **120**, 1421 (2016). doi:10.1021/acs.jpcc.5b11451.

[43] G. Talasila, S. Sachdev, U. Srivastva, D. Saxena, and S. S. V. Ramakumar, *Modified Synthesis of $BiVO_4$ and Effect of Doping (Mo or W) on Its Photoelectrochemical Performance for Water Splitting,* Energy Reports **6**, 1963 (2020). doi:10.1016/j.egyr.2020.07.024.

[44] C. Zhou, Z. Sanders-Bellis, T. J. Smart, W. Zhang, L. Zhang, Y. Ping, and M. Liu, *Interstitial Lithium Doping in $BiVO_4$ Thin Film Photoanode for Enhanced Solar Water Splitting Activity,* Chem. Mater. **32**, 6401 (2020). doi:10.1021/acs.chemmater.0c01481.

[45] F. F. Abdi, T. J. Savenije, M. M. May, B. Dam, and R. van de Krol, *The Origin of Slow Carrier Transport in $BiVO_4$ Thin Film Photoanodes: A Time-Resolved Microwave Conductivity Study,* J. Phys. Chem. Lett. **4**, 2752 (2013). doi:10.1021/jz4013257.

[46] T. W. Kim, Y. Ping, G. A. Galli, and K.-S. Choi, *Simultaneous Enhancements in Photon Absorption and Charge Transport of Bismuth Vanadate Photoanodes for Solar Water Splitting,* Nat Commun **6**, 8769 (2015). doi:10.1038/ncomms9769.

[47] R. Irani, I. Y. Ahmet, J.-W. Jang, S. P. Berglund, P. Plate, C. Höhn, R. Böttger, S. W. Schmitt, C. Dubourdieu, S. Lardhi, L. Cavallo, M. Harb, P. Bogdanoff, R. van de Krol, and F. F. Abdi, *Nature of Nitrogen Incorporation in $BiVO_4$ Photoanodes through Chemical and Physical Methods,* Sol. RRL **4**, 1900290 (2020). doi:10.1002/solr.201900290.

[48] S. Wang, X. Wang, B. Liu, Z. Guo, K. K. Ostrikov, L. Wang, and W. Huang, *Vacancy Defect Engineering of $BiVO_4$ Photoanodes for Photoelectrochemical Water Splitting,* Nanoscale **13**, 17989 (2021). doi:10.1039/D1NR05691C.

[49] S. Wang, P. Chen, Y. Bai, J.-H. Yun, G. Liu, and L. Wang, *New $BiVO_4$ Dual Photoanodes with Enriched Oxygen Vacancies for Efficient Solar-Driven Water Splitting,* Adv. Mater. **30**, 1800486 (2018). doi:10.1002/adma.201800486.

[50] W. Zhang, L. Song, J. Cen, and M. Liu, *Mechanistic Insights into Defect-Assisted Carrier Transport in Bismuth Vanadate Photoanodes,* J. Phys. Chem. C **123**, 20730 (2019). doi:10.1021/acs.jpcc.9b04583.

[51] S. Wang, T. He, P. Chen, A. Du, K. K. Ostrikov, W. Huang, and L. Wang, *In Situ Formation of Oxygen Vacancies Achieving Near-Complete Charge Separation in Planar $BiVO_4$ Photoanodes,* Adv. Mater. **32**, 2001385 (2020). doi:10.1002/adma.202001385.

[52] M. D. Rossell, P. Agrawal, A. Borgschulte, C. Hébert, D. Passerone, and R. Erni, *Direct Evidence of Surface Reduction in Monoclinic $BiVO_4$,* Chem. Mater. **27**, 3593 (2015). doi:10.1021/cm504248d.

[53] M. Lamers, S. Fiechter, D. Friedrich, F. F. Abdi, and R. van de Krol, *Formation and Suppression of Defects during Heat Treatment of $BiVO_4$ Photoanodes for Solar Water Splitting,* Journal of Materials Chemistry A **6**, 18694 (2018). doi:10.1039/C8TA06269B.

[54] W. Qiu, S. Xiao, J. Ke, Z. Wang, S. Tang, K. Zhang, W. Qian, Y. Huang, D. Huang, Y. Tong, and S. Yang, *Freeing the Polarons to Facilitate Charge Transport in $BiVO_4$ from Oxygen Vacancies with an Oxidative 2D Precursor,* Angew. Chem. Int. Ed. **58**, 19087 (2019). doi:10.1002/anie.201912475.

[55] X. Zhao, J. Hu, X. Yao, S. Chen, and Z. Chen, *Clarifying the Roles of Oxygen Vacancy in W-Doped $BiVO_4$ for Solar Water Splitting,* ACS Appl. Energy Mater. **1**, 3410 (2018). doi:10.1021/acsaem.8b00559.

[56] F. S. Hegner, D. Forrer, J. R. Galán-Mascarós, N. López, and A. Selloni, *Versatile Nature of Oxygen Vacancies in Bismuth Vanadate Bulk and (001) Surface,* J. Phys. Chem. Lett. **10**, 6672 (2019). doi:10.1021/acs.jpclett.9b02552.

[57] W. Wang, P. J. Strohbeen, D. Lee, C. Zhou, J. K. Kawasaki, K.-S. Choi, M. Liu, and G. Galli, *The Role of Surface Oxygen Vacancies in $BiVO_4$,* Chem. Mater. **32**, 2899 (2020). doi:10.1021/acs.chemmater.9b05047.

[58] X. Rong, J. Parolin, and A. M. Kolpak, *A Fundamental Relationship between Reaction Mechanism and Stability in Metal Oxide Catalysts for Oxygen Evolution,* ACS Catal. **6**, 1153 (2016). doi:10.1021/acscatal.5b02432.

[59] A. Grimaud, O. Diaz-Morales, B. Han, W. T. Hong, Y.-L. Lee, L. Giordano, K. A. Stoerzinger, M. T. M. Koper, and Y. Shao-Horn, *Activating Lattice Oxygen Redox Reactions in Metal Oxides to Catalyse Oxygen Evolution,* Nature Chem **9**, 457 (2017). doi:10.1038/nchem.2695.

[60] Y. Hermans, S. Murcia-López, A. Klein, and W. Jaegermann, *$BiVO_4$ Surface Reduction upon Water Exposure,* ACS Energy Lett. **4**, 2522 (2019). doi:10.1021/acsenergylett.9b01667.

[61] P. Nikačević, F. S. Hegner, J. R. Galán-Mascarós, and N. López, *Influence of Oxygen Vacancies and Surface Facets on Water Oxidation Selectivity toward Oxygen or Hydrogen Peroxide with $BiVO_4$,* ACS Catal. , 13416 (2021). doi:10.1021/acscatal.1c03256.

[62] Y. Lu, Y. Yang, X. Fan, Y. Li, D. Zhou, B. Cai, L. Wang, K. Fan, and K. Zhang, *Boosting Charge Transport in $BiVO_4$ Photoanode for Solar Water Oxidation,* Advanced Materials **34**, 2108178 (2022). doi:10.1002/adma.202108178.

[63] W.-J. Yin, S.-H. Wei, M. M. Al-Jassim, J. Turner, and Y. Yan, *Doping Properties of Monoclinic $BiVO_4$ Studied by First-Principles Density-Functional Theory,* Phys. Rev. B **83**, 155102 (2011). doi:10.1103/PhysRevB.83.155102.

[64] J. Zhang, X. Chen, M. Deng, H. Shen, H. Li, and J. Ding, *Effects of Native Defects and Cerium Impurity on the Monoclinic $BiVO_4$ Photocatalyst Obtained via PBE+U Calculations,* Phys. Chem. Chem. Phys. **22**, 25297 (2020). doi:10.1039/D0CP01983F.

[65] N. Österbacka, F. Ambrosio, and J. Wiktor, *Charge Localization in Defective $BiVO_4$,* J. Phys. Chem. C **126**, 2960 (2022). doi:10.1021/acs.jpcc.1c09990.

[66] T. Tran-Phu, Z. Fusco, I. Di Bernardo, J. Lipton-Duffin, C. Y. Toe, R. Daiyan, T. Gengenbach, C.-H. Lin, R. Bo, H. T. Nguyen, G. M. J. Barca, T. Wu, H. Chen, R. Amal, and A. Tricoli, *Understanding the Role of Vanadium Vacancies in $BiVO_4$ for Efficient Photoelectrochemical Water Oxidation,* Chem. Mater. , (2021). doi:10.1021/acs.chemmater.0c04866.

[67] D. K. Lee and K.-S. Choi, *Enhancing Long-Term Photostability of $BiVO_4$ Photoanodes for Solar Water Splitting by Tuning Electrolyte Composition,* Nat Energy **3**, 53 (2018). doi:10.1038/s41560-017-0057-0.

[68] A. J. E. Rettie, W. D. Chemelewski, J. Lindemuth, J. S. McCloy, L. G. Marshall, J. Zhou, D. Emin, and C. B. Mullins, *Anisotropic Small-Polaron Hopping in W:$BiVO_4$ Single Crystals,* Appl. Phys. Lett. **106**, 022106 (2015). doi:10.1063/1.4905786.

[69] M. Ziwritsch, S. Müller, H. Hempel, T. Unold, F. F. Abdi, R. van de Krol, D. Friedrich, and R. Eichberger, *Direct Time-Resolved Observation of Carrier Trapping and Polaron Con-*

ductivity in $BiVO_4$, ACS Energy Lett. **1**, 888 (2016). doi:10.1021/acsenergylett.6b00423.

[70] A. J. E. Rettie, W. D. Chemelewski, D. Emin, and C. B. Mullins, *Unravelling Small-Polaron Transport in Metal Oxide Photoelectrodes,* J. Phys. Chem. Lett. **7**, 471 (2016). doi:10.1021/acs.jpclett.5b02143.

[71] J. Wiktor, F. Ambrosio, and A. Pasquarello, *Role of Polarons in Water Splitting: The Case of $BiVO_4$,* ACS Energy Lett. **3**, 1693 (2018). doi:10.1021/acsenergylett.8b00938.

[72] H. Seo, Y. Ping, and G. Galli, *Role of Point Defects in Enhancing the Conductivity of $BiVO_4$,* Chem. Mater. **30**, 7793 (2018). doi:10.1021/acs.chemmater.8b03201.

[73] J. K. Cooper, S. B. Scott, Y. Ling, J. Yang, S. Hao, Y. Li, F. M. Toma, M. Stutzmann, K. V. Lakshmi, and I. D. Sharp, *Role of Hydrogen in Defining the N-Type Character of $BiVO_4$ Photoanodes,* Chem. Mater. **28**, 5761 (2016). doi:10.1021/acs.chemmater.6b01994.

[74] H. L. Tan, A. Suyanto, A. T. D. Denko, W. H. Saputera, R. Amal, F. E. Osterloh, and Y. H. Ng, *Enhancing the Photoactivity of Faceted $BiVO_4$ via Annealing in Oxygen-Deficient Condition,* Part. Part. Syst. Charact. **34**, 1600290 (2017). doi:10.1002/ppsc.201600290.

[75] S. Selim, E. Pastor, M. García-Tecedor, M. R. Morris, L. Francàs, M. Sachs, B. Moss, S. Corby, C. A. Mesa, S. Gimenez, A. Kafizas, A. A. Bakulin, and J. R. Durrant, *Impact of Oxygen Vacancy Occupancy on Charge Carrier Dynamics in $BiVO_4$ Photoanodes,* J. Am. Chem. Soc. **141**, 18791 (2019). doi:10.1021/jacs.9b09056.

[76] S. Byun, G. Jung, Y. Shi, M. Lanza, and B. Shin, *Aging of a Vanadium Precursor Solution: Influencing Material Properties and Photoelectrochemical Water Oxidation Performance of Solution-Processed $BiVO_4$ Photoanodes,* Adv. Funct. Mater. **30**, 1806662 (2020). doi:10.1002/adfm.201806662.

[77] N. Österbacka and J. Wiktor, *Influence of Oxygen Vacancies on the Structure of $BiVO_4$,* J. Phys. Chem. C **125**, 1200 (2021). doi:10.1021/acs.jpcc.0c08751.

[78] F. Giustino, *Materials Modelling Using Density Functional Theory: Properties and Predictions* (Oxford: Oxford University Press, 2014). ISBN 978-0-19-966243-2 978-0-19-966244-9.

[79] F. Jensen, *Introduction to Computational Chemistry* (Chichester, UK ; Hoboken, NJ: Wiley, 2017). ISBN 978-1-118-82595-2 978-1-118-82598-3.

[80] W. Koch and M. C. Holthausen, *A Chemist's Cuide to Density Functional Theory* (Weinheim: Wiley-VCH, 2001). ISBN 978-3-527-30372-4 978-3-527-30422-6.

[81] M. Born and R. Oppenheimer, *Zur Quantentheorie Der Molekeln,* Annalen der Physik **389**, 457 (1927). doi:10.1002/andp.19273892002.

[82] P. Hohenberg and W. Kohn, *Inhomogeneous Electron Gas,* Phys. Rev. **136**, B864 (1964). doi:10.1103/PhysRev.136.B864.

[83] W. Kohn and L. J. Sham, *Self-Consistent Equations Including Exchange and Correlation Effects,* Phys. Rev. **140**, A1133 (1965). doi:10.1103/PhysRev.140.A1133.

[84] J. P. Perdew and K. Burke, *Comparison Shopping for a Gradient-Corrected Density Functional,* Int. J. Quantum Chem. **57**, 309 (1996). doi:10.1002/(SICI)1097-461X(1996)57:3<309::AID-QUA4>3.0.CO;2-1.

[85] J. P. Perdew, K. Burke, and M. Ernzerhof, *Generalized Gradient Approximation Made Simple,* Phys. Rev. Lett. 77, 3865 (1996). doi:10.1103/PhysRevLett.77.3865.

[86] N. Mardirossian and M. Head-Gordon, *Thirty Years of Density Functional Theory in Computational Chemistry: An Overview and Extensive Assessment of 200 Density Functionals,* Mol. Phys. **115**, 2315 (2017). doi:10.1080/00268976.2017.1333644.

[87] P. Haas, F. Tran, P. Blaha, K. Schwarz, and R. Laskowski, *Insight into the Performance of GGA Functionals for Solid-State Calculations,* Phys. Rev. B **80**, 195109 (2009). doi:10.1103/PhysRevB.80.195109.

[88] A. J. Cohen, P. Mori-Sánchez, and W. Yang, *Insights into Current Limitations of Density Functional Theory,* Science , (2008). doi:10.1126/science.1158722.

[89] A. J. Cohen, P. Mori-Sánchez, and W. Yang, *Fractional Charge Perspective on the Band Gap in Density-Functional Theory,* Phys. Rev. B 77, 115123 (2008). doi:10.1103/PhysRevB.77.115123.

[90] P. Mori-Sánchez, A. J. Cohen, and W. Yang, *Localization and Delocalization Errors in Density Functional Theory and Implications for Band-Gap Prediction,* Phys. Rev. Lett. **100**, 146401 (2008). doi:10.1103/PhysRevLett.100.146401.

[91] J. P. Perdew and A. Zunger, *Self-Interaction Correction to Density-Functional Approximations for Many-Electron Systems,* Phys. Rev. B **23**, 5048 (1981). doi:10.1103/PhysRevB.23.5048.

[92] B. Sadigh, P. Erhart, and D. Åberg, *Variational Polaron Self-Interaction-Corrected Total-Energy Functional for Charge Excitations in Insulators,* Phys. Rev. B **92**, 075202 (2015). doi:10.1103/PhysRevB.92.075202.

[93] A. D. Becke, *A New Mixing of Hartree–Fock and Local Density-functional Theories,* J. Chem. Phys. **98**, 1372 (1993). doi:10.1063/1.464304.

[94] J. P. Perdew, M. Ernzerhof, and K. Burke, *Rationale for Mixing Exact Exchange with Density Functional Approximations,* J. Chem. Phys. **105**, 9982 (1996). doi:10.1063/1.472933.

[95] C. Adamo and V. Barone, *Toward Reliable Density Functional Methods without Adjustable Parameters: The PBE0 Model,* J. Chem. Phys. **110**, 6158 (1999). doi:10.1063/1.478522.

[96] J. P. Perdew, R. G. Parr, M. Levy, and J. L. Balduz, *Density-Functional Theory for Fractional Particle Number: Derivative Discontinuities of the Energy,* Phys. Rev. Lett. **49**, 1691 (1982). doi:10.1103/PhysRevLett.49.1691.

[97] J. P. Perdew and M. Levy, *Physical Content of the Exact Kohn-Sham Orbital Energies: Band Gaps and Derivative Discontinuities,* Phys. Rev. Lett. **51**, 1884 (1983). doi:10.1103/PhysRevLett.51.1884.

[98] G. Miceli, W. Chen, I. Reshetnyak, and A. Pasquarello, *Nonempirical Hybrid Functionals for Band Gaps and Polaronic Distortions in Solids,* Phys. Rev. B **97**, 121112 (2018). doi:10.1103/PhysRevB.97.121112.

[99] K. Lejaeghere, V. Van Speybroeck, G. Van Oost, and S. Cottenier, *Error Estimates for Solid-State Density-Functional Theory Predictions: An Overview by Means of the Ground-State Elemental Crystals,* Critical Reviews in Solid State and Materials Sciences **39**, 1 (2014). doi:10.1080/10408436.2013.772503.

[100] T. D. Kühne, M. Iannuzzi, M. Del Ben, V. V. Rybkin, P. Seewald, F. Stein, T. Laino, R. Z. Khaliullin, O. Schütt, F. Schiffmann, D. Golze, J. Wilhelm, S. Chulkov, M. H. Bani-Hashemian, V. Weber, U. Borštnik, M. Taillefumier, A. S. Jakobovits, A. Lazzaro, H. Pabst, T. Müller, R. Schade, M. Guidon, S. Andermatt, N. Holmberg, G. K. Schenter, A. Hehn, A. Bussy, F. Belleflamme, G. Tabacchi, A. Glöß, M. Lass, I. Bethune, C. J. Mundy, C. Plessl, M. Watkins, J. VandeVondele, M. Krack, and J. Hutter, *CP2K: An Electronic Structure and Molecular Dynamics Software Package - Quickstep: Efficient and Accurate Electronic Structure Calculations,* J. Chem. Phys. **152**, 194103 (2020). doi:10.1063/5.0007045.

[101] G. Lippert, J. Hutter, and M. Parrinello, *A Hybrid Gaussian and Plane Wave Density Functional Scheme,* Mol. Phys. **92**, 477 (1997). doi:10.1080/00268979709482119.

[102] J. VandeVondele, M. Krack, F. Mohamed, M. Parrinello, T. Chassaing, and J. Hutter, *Quickstep: Fast and Accurate Density Functional Calculations Using a Mixed Gaussian and Plane Waves Approach,* Computer Physics Communications **167**, 103 (2005). doi:10.1016/j.cpc.2004.12.014.

[103] J. Spencer and A. Alavi, *Efficient Calculation of the Exact Exchange Energy in Periodic Systems Using a Truncated Coulomb Potential,* Phys. Rev. B 77, 193110 (2008). doi:10.1103/PhysRevB.77.193110.

[104] M. Guidon, J. Hutter, and J. VandeVondele, *Robust Periodic Hartree-Fock Exchange for Large-Scale Simulations Using Gaussian Basis Sets,* J. Chem. Theory Comput. **5**, 3010 (2009). doi:10.1021/ct900494g.

[105] M. Guidon, J. Hutter, and J. VandeVondele, *Auxiliary Density Matrix Methods for Hartree-Fock Exchange Calculations,* J. Chem. Theory Comput. **6**, 2348 (2010). doi:10.1021/ct1002225.

[106] H.-P. Komsa, T. T. Rantala, and A. Pasquarello, *Finite-Size Supercell Correction Schemes for Charged Defect Calculations,* Phys. Rev. B **86**, 045112 (2012). doi:10.1103/PhysRevB.86.045112.

[107] C. Freysoldt, B. Grabowski, T. Hickel, J. Neugebauer, G. Kresse, A. Janotti, and C. G. Van de Walle, *First-Principles Calculations for Point Defects in Solids,* Rev. Mod. Phys. **86**, 253 (2014). doi:10.1103/RevModPhys.86.253.

[108] S. Lany and A. Zunger, *Assessment of Correction Methods for the Band-Gap Problem and for Finite-Size Effects in Supercell Defect Calculations: Case Studies for ZnO and GaAs,* Phys. Rev. B **78**, 235104 (2008). doi:10.1103/PhysRevB.78.235104.

[109] M. Leslie and N. J. Gillan, *The Energy and Elastic Dipole Tensor of Defects in Ionic Crystals Calculated by the Supercell Method,* J. Phys. C: Solid State Phys. **18**, 973 (1985). doi:10.1088/0022-3719/18/5/005.

[110] C. Freysoldt, J. Neugebauer, and C. G. Van de Walle, *Fully Ab Initio Finite-Size Corrections for Charged-Defect Supercell Calculations,* Phys. Rev. Lett. **102**, 016402 (2009). doi:10.1103/PhysRevLett.102.016402.

[111] C. Freysoldt, J. Neugebauer, and C. G. V. de Walle, *Electrostatic Interactions between Charged Defects in Supercells,* Phys. Status Solidi B **248**, 1067 (2011). doi:10.1002/pssb.201046289.